1290

UNIVERSIDADE DE
COIMBRA

Gil Vilela Probst

AB INITIO STUDY OF 2D SUPERCONDUCTORS

VOLUME 1

Dissertação no âmbito da Física da Matéria Condensada orientada pelo Doutor Tiago Frederico Teixeira Cerqueira e Doutor Pedro Miguel de Castro Borlido apresentada ao Departamento de Física da Faculdade de Ciências e Tecnologia da Universidade de Coimbra.

Setembro de 2023

Ab Initio Study of 2D Superconductors

Gil Vilela Probst

Department of Physics
University of Coimbra

A thesis submitted for the degree of
Master in Physics

Coimbra, 11th September 2023

Acknowledgements

I am deeply thankful to my supervisors Tiago Cerqueira and Pedro Borlido for teaching, guiding and mentoring me throughout this year. Their help was crucial not only for this thesis but also for the two seminars and one poster I had to prepare this year. Special thanks to Fernando Nogueira for mentoring and supervising this thesis as well as helping me present the two seminars and one poster this year. In my many years at the University of Coimbra I had the pleasure to be a student of Professor Nogueira multiple times and see first hand his exceptional teaching skills and his connection with the students. Special thanks to my mother for everything. Special thanks to my friends especially to Margarida Santiago for her unwavering support, Giorgio Canezin for his companionship, Daniel Neves, Tânia Sousa and Felipe Pereira for their friendship as well as productive and insightful discussions on physics and life in general.

Abstract

The first successful synthesis of graphene reported in 2004 spawned a new gold rush for 2D materials. This class of materials is of high interest due to their many envisioned technological applications. One of these applications, that is studied in this thesis, is their potential as superconductors. The work done for this thesis consisted of determining the ideal parameters for a broad database search. This was only the first step to effectively screen a database of 2D materials for potential superconductors. To research the superconductivity in this 2D environment five new theoretical 2D materials with a high electronic occupancy at the Fermi level were selected and studied with DFT. Their critical transition temperatures were estimated based on the Migdal-Eliashberg formalism. The obtained transition temperatures ranged from 0.4 K to 3.4 K.

Resumo

A primeira síntese bem-sucedida de grafeno, relatada em 2004, gerou uma nova procura extensiva para materiais 2D. Esta classe de materiais é de grande interesse devido às suas muitas características e aplicações tecnológicas. Uma dessas aplicações, que é estudada nesta tese, é o seu potencial como supercondutores. A supercondutividade tem sido pesquisada há mais de 100 anos, porém os supercondutores mais utilizados atualmente são ainda compostos metálicos à base de nióbio descobertos na década de 60. O trabalho realizado para esta tese consistiu em determinar os parâmetros ideais para uma ampla pesquisa em bases de dados. Este foi apenas o primeiro passo para rastrear efetivamente uma base de dados de materiais 2D para possíveis supercondutores. Para pesquisar a supercondutividade neste ambiente 2D cinco novos materiais 2D teóricos com alta ocupação eletrónica no nível de Fermi foram selecionados e estudados com DFT. As suas temperaturas críticas de transição foram estimadas com base no formalismo de Migdal-Eliashberg. As temperaturas de transição obtidas variaram entre 0,4 K e 3,4 K.

Table of contents

Chapter 1

Motivation

Superconductivity continues to be one of the most researched topics in condensed matter physics today despite the phenomenon itself being discovered more than 100 years ago [1]. The reasons for this are many, but four of them will be highlighted here: 1) Many, but not all superconductors are well understood and described by Bardeen-Cooper-Schrieffer (BCS) and Migdal-Eliashberg (ME) theories in terms of their superconducting mechanism. Those that are not described by the electron-phonon mechanism of BCS and ME are labelled unconventional superconductors. Many of these do not yet have a concrete theoretical model to explain their superconductivity and predict their transition temperature. Unconventional superconductivity came into the limelight with the discovery of several high critical temperature (T_c) cuprate-class (copper oxides) superconductors in the 80's. More recently iron-based and carbon-based superconductors have been researched. 2) The potential discovery of an ambient temperature, low pressure, ductile and cheap superconductor would be extraordinarily useful, allowing for efficient energy transportation, storage and use. This makes the rewards for successful research in this field clear. Sadly, no single material discovered so far has anywhere near all the properties mentioned above. The vast majority of superconductors have low transition temperatures and a lot of the high T_c ones require high pressures on the order of GPa or are very brittle which is problematic when the goal is to make wires with them. In spite of decades of research the most used superconductors today are still niobium based compounds discovered in the 50's. 3) Computationally predicting a material's viability as a superconductor with a satisfactory degree of confidence is slow and expensive. This problem is compounded by the fact that there are many hundreds' of thousands of materials yet to be tested. Methods to predict a materials' superconductive properties require computationally expensive electron-phonon calculations. 4) Even if a material with a computationally obtained high T_c and small energy above convex hull is found, it may not be synthesizable in a laboratory or have a economically viable use. The convex hull is an energy plot where different phases of the same material are plotted. The formation energy of each is represented by the y direction and the concentration of a particular element is shown in the x direction. Stable phases of the compound are linked by straight lines. Metastable or unstable phases of the compound lie above this line. In theory the smaller the formation energy difference between a given phase and the point on the convex hull directly below it the more likely it is that the phase is synthesizable.

The turn of the millennium yielded an explosion in scientific interest and research into single-layer materials. The first successful synthesis of graphene and measurement of it's very high electrical conductivity and tensile strength [2] won Andrei Geim and Konstantin Novoselov the 2010 Nobel prize in physics. Since then, research on this class of materials has continued due to their potential applications as electronic devices, photon detectors and solar cells [3]. This recent interest in 2D materials, the increase in computational power available and the existence of accurate electronic structure methods such as Density Functional Theory (DFT) make it now possible to create large databases of thousands of stable 2D materials, as shown in [4] and [5].

Nowadays it is possible to accurately study the conventional superconductivity of a material using DFT in an efficient manner. To this end, a number of materials were selected and studied to better understand the optimal parameters for a broad database search. Knowing the most optimal way of conducting this search will make it possible to efficiently screen many databases of 2D materials for a good superconductors with confidence that the obtained results are accurate.

This thesis is structured in six Chapters, this motivation being the first one. The other five Chapters numbered 2 through 6 cover the following topics: Theoretical overview of DFT with a discussion on exchange-correlation approximations and superconductivity; Review of 2D materials; Methodology used for the main work and the first tests; Results and discussion; Conclusions and future work.

Chapter 2

Theoretical Overview of the Many-body Problem in the Framework of Density Functional Theory, Exchange-Correlation Approximations and Superconductivity

2.1 Many Body Schrödinger Equation

The non-relativistic many body Schrödinger equation describes a system of N electrons and M nuclei with masses m_I and charges Z_I. The electron's coordinates are $\mathbf{r}_i$ while those for the nuclei are $\mathbf{R}_I$. Writing the Hamiltonian in atomic units ($\hbar = m_e = \frac{e^2}{4\pi\epsilon_0} = 1$) we get,

$$H(\mathbf{r_1}, ..., \mathbf{r_N}, \mathbf{R_1}, ..., \mathbf{R_M}) = -\sum_{i=1}^{N} \frac{\nabla_i^2}{2} - \sum_{I=1}^{M} \frac{\nabla_I^2}{2m_I} \tag{2.1}$$

$$-\sum_{i,I=1}^{N,M} \frac{Z_I}{|\mathbf{r_i} - \mathbf{R_I}|} + \sum_{i,j=1\&i<j}^{N} \frac{1}{|\mathbf{r_i} - \mathbf{r_j}|} + \sum_{I,J=1\&I<J}^{M} \frac{Z_I Z_J}{|\mathbf{R_I} - \mathbf{R_J}|} \ .$$

This can be simplified using the Born-Oppenheimer approximation [6]. This approximation takes advantage of the fact that the nuclei move much more slowly than the electrons due to them being thousands of times more massive. Due to this, equation (2.1) can then be separated into a electronic Hamiltonian and a nuclear Hamiltonian.

In the first one the electronic wavefunction depends parametrically, not explicitly, on the nuclear coordinates. This means that for different nuclear arrangements the electronic function is a different function of the electronic coordinates. The total wave function from the Schrödinger equation is separated.

$$\Psi(\mathbf{r_1},...,\mathbf{r_N},\mathbf{R_1},...,\mathbf{R_M}) = \Phi_{\text{elec}}(\mathbf{r_1},...,\mathbf{r_N},\mathbf{R_1},...,\mathbf{R_M})\Phi_{\text{nucl}}(\mathbf{R_1},...,\mathbf{R_M}) \tag{2.2}$$

We then get two separate equations, one for the electrons,

$$\left(-\sum_{i=1}^{N}\frac{\nabla_i^2}{2} + \sum_{i,j=1\&i<j}^{N}\frac{1}{|\mathbf{r_i}-\mathbf{r_j}|} - \sum_{i,I=1}^{N,M}\frac{Z_I}{|\mathbf{r_i}-\mathbf{R_I}|}\right)\Phi_{\text{elec}}(\mathbf{r_1},...,\mathbf{r_N},\{\mathbf{R_1},...,\mathbf{R_M}\}) \tag{2.3}$$

$$= E_{\text{elec}}(\mathbf{R_1},...,\mathbf{R_M})\Phi_{\text{elec}}(\mathbf{r_1},...,\mathbf{r_N},\{\mathbf{R_1},...,\mathbf{R_M}\})$$

and another for the nuclei,

$$\left(-\sum_{I=1}^{M}\frac{\nabla_I^2}{2m_I} + E_{\text{elec}}(\mathbf{R_1},...,\mathbf{R_M}) + \sum_{I,J=1\&I<J}^{M}\frac{Z_IZ_J}{|\mathbf{R_I}-\mathbf{R_J}|}\right)\Phi_{\text{nucl}}(\mathbf{R_1},...,\mathbf{R_M}) \tag{2.4}$$

$$= E\Phi(\mathbf{R_1},...,\mathbf{R_M})$$

2.2 Density Functional Theory

In 1964, the year collectively considered to be the birth year of Density Functional Theory (DFT), Pierre Hohenberg and Walter Kohn published a joint paper [7]. In this seminal work, they formulated a new model to treat the problem of a gas of interacting electrons in some external multiplicative potential $\nu(\mathbf{r})$. They showed that: "For any N-electron system the external potential $\nu(\mathbf{r})$ is (to within a constant) a unique functional of the ground state density $\rho_0(\mathbf{r})$; since, in turn, $\nu(\mathbf{r})$ fixes $\hat{H}$ we see that the full many-particle Hamiltonian $\hat{H}$ is a unique functional of $\rho_0(\mathbf{r})$." Meaning that there is a one-to-one correspondence between the potential and the ground-state electron density.

$$\{\nu\} \longleftrightarrow \{\Psi\} \longleftrightarrow \{\rho\} \tag{2.5}$$

They also proved that "The energy functional $E_\nu[\rho] = \int \nu(\mathbf{r})\rho(\mathbf{r})d\mathbf{r} + F[\rho]$ assumes it's minimum for the ground state density $\rho_0(\mathbf{r})$." Where $F[\rho]$ is an universal functional i.e., it's the same functional for any N-electron system.

In the following year Walter Kohn and Lu Jeu Sham published a joint paper [8] suggesting a method to yield a set of self-consistent equations for the ground-state energy that can be computed iteratively. These equations we know today as the Kohn-Sham equations, the basis of all DFT programs. Walter Kohn went on to win the 1998 Nobel Prize in Chemistry for these equations.

2.3 Hohenberg-Kohn Theorem

For the system under study in this work, the N-electron non-relativistic time-independent Hamiltonian is in standard notation,

$$\hat{H} = \hat{T} + \hat{V} + \hat{W} \tag{2.6}$$

Let's consider a set $\mathcal{V}$ of local one-electron external potentials $\hat{V}$ for which $\hat{H}$ has a non-degenerate ground state.

$$\hat{H}\left|\mathit{\Psi}\right\rangle = (\hat{T} + \hat{V} + \hat{W})\left|\mathit{\Psi}\right\rangle = E_{\text{gs}}\left|\mathit{\Psi}\right\rangle \qquad \hat{V} \in \mathcal{V} \tag{2.7}$$

These ground states $\left|\mathit{\Psi}\right\rangle$ can be condensed into another set Ψ, the set of all ground states, creating the map

$$C : \mathcal{V} \to \Psi \tag{2.8}$$

If we look at the electronic density of all the ground-state wavefunctions in $\mathit{\Psi}$:

$$\rho(\mathbf{r}) = N \sum_{\alpha} \int d\mathbf{x_2} \ldots \int d\mathbf{x}_N \left|\mathit{\Psi}\left(\mathbf{r}_\alpha, \mathbf{x}_2, \ldots, \mathbf{x}_N\right)\right|^2 \tag{2.9}$$

where we are summing over both spins denominated by α this establishes another map,

$$D : \Psi \to \mathcal{N} \tag{2.10}$$

between the set of all ground-state wavefunctions and the set of all ground-state densities.

We can easily see that the map DC $\mathcal{V} \to \mathcal{N}$ indicates a relation between external potentials and ground-state densities. But is this a one-to-one relation?

Proving that there is a one-to-one correspondence between the electron density and the potential requires a proof of injectivity of the maps C and D.

Starting with map C, consider two states. The first, $|\Psi\rangle$, is a ground state of $\hat{V}$ and has energy E_{gs}. The second $|\Psi'\rangle$, is a ground state of $\hat{V'}$ and has energy E'_{gs}. If the potentials differ by more than a constant then,

$$\hat{V} \neq \hat{V}' + \text{Const} \tag{2.11}$$

$$(\hat{T} + \hat{V} + \hat{W})\,|\Psi\rangle = E_{\text{gs}}\,|\Psi\rangle \tag{2.12}$$

$$(\hat{T} + \hat{V}' + \hat{W})\,|\Psi'\rangle = E'_{\text{gs}}\,|\Psi'\rangle \tag{2.13}$$

If $|\Psi\rangle = |\Psi'\rangle$ then,

$$(\hat{V} - \hat{V}')\,|\Psi\rangle = (E_{\text{gs}} - E'_{\text{gs}})\,|\Psi\rangle \tag{2.14}$$

leading to, $(\hat{V} - \hat{V}') = (E_{\text{gs}} - E'_{\text{gs}})$, which contradicts equation (2.11). As we can see, if two ground states are equal than this implies that their potentials only differ by a constant at most. Therefore the map C is injective, there is a one-to-one correspondence between the two sets of the map. For map D we need to show that different ground-state wavefunctions $|\Psi\rangle$ and $|\Psi'\rangle$, corresponding to ground-states for different external potentials imply different densities $\rho_0(\mathbf{r})$ and $\rho'_0(\mathbf{r})$. Suppose that

$$E_{\text{gs}} = \langle\Psi|\,\hat{H}\,|\Psi\rangle < \langle\Psi'|\,\hat{H}\,|\Psi'\rangle \tag{2.15}$$

and by the Rayleigh-Ritz principle,

$$\langle\Psi'|\,\hat{H}\,|\Psi'\rangle = \langle\Psi'|\,(\hat{H}' + \hat{V} - \hat{V}')\,|\Psi'\rangle = E'_{\text{gs}} + \int \rho'_0(\mathbf{r})[\nu(\mathbf{r}) - \nu'(\mathbf{r})]d^3r \tag{2.16}$$

$$E_{\text{gs}} < E'_{\text{gs}} + \int \rho'_0(\mathbf{r})[\nu(\mathbf{r}) - \nu'(\mathbf{r})]d^3r \tag{2.17}$$

likewise for E'_{gs},

$$E'_{\text{gs}} = \langle\Psi'|\,\hat{H}'\,|\Psi'\rangle < \langle\Psi|\,\hat{H}'\,|\Psi\rangle \tag{2.18}$$

$$\langle \Psi | \hat{H}' | \Psi \rangle = \langle \Psi | (\hat{H} + \hat{V}' - \hat{V}) | \Psi \rangle = E_{\text{gs}} + \int \rho_0(\mathbf{r})[\nu'(\mathbf{r}) - \nu(\mathbf{r})] d^3r \tag{2.19}$$

$$E'_{\text{gs}} < E_{\text{gs}} + \int \rho_0(\mathbf{r})[\nu'(\mathbf{r}) - \nu(\mathbf{r})] d^3r \tag{2.20}$$

assuming that $\rho_0(\mathbf{r}) = \rho'_0(\mathbf{r})$ and combining equations (2.17) and equation (2.20) yields,

$$E_{\text{gs}} + E'_{\text{gs}} < E_{\text{gs}} + E'_{\text{gs}}. \tag{2.21}$$

With this contradiction, it is shown that different ground states must have different densities. Therefore the map D is bijective (it has a reversible one-to-one correspondence).

$$D^{-1} : \rho_0(\mathbf{r}) \to |\Psi[\rho_0]\rangle \tag{2.22}$$

Now armed with this knowledge we can formulate the first statement of the theorem, there is a one-to-one correspondence between the potential and the ground-state electron density. The ground state expectation value of any observable $\hat{A}$ is a unique functional of the exact ground state density ρ.

$$\langle \Psi[\rho] | \hat{A} | \Psi[\rho] \rangle = A[\rho] \tag{2.23}$$

The inverse of maps C and D is

$$(DC)^{-1} : \rho_0(\mathbf{r}) \to \nu(\mathbf{r}) \tag{2.24}$$

and shows that the ground-state density ρ_0 uniquely determines the external potential $\nu(\mathbf{r})$.

Secondly, we must show the variational character of the Hamiltonian. Consider a system with a ground state external potential $\hat{V}_0$ and a ground state density $\rho_0(\mathbf{r})$ with energy E_{ν_0}.

$$E_{\nu_0}[\rho_0] = \langle \Psi[\rho_0] | (\hat{T} + \hat{V}_0 + \hat{W}) | \Psi[\rho_0] \rangle \tag{2.25}$$

This creates the universal (meaning that it is the same regardless of the N-electron system considered) energy functional $F_{HK}[\rho]$,

$$F_{HK}[\rho] = \langle \Psi[\rho] | (\hat{T} + \hat{W}) | \Psi[\rho] \rangle \tag{2.26}$$

$$E_{\nu_0}[\rho] = F_{HK}[\rho] + \int \nu_0(\mathbf{r})\rho(\mathbf{r})d^3r \tag{2.27}$$

In 1982 the Hohenberg Theorem was expanded to include degenerate ground states [9] [10].

As shown previously, the states $\Psi[\rho]$ are generated with the inverse D map from the set $\mathcal{N}$. By the Rayleigh-Ritz principle,

$$E_0 < E_{\nu_0}[\rho] \text{ for } \rho \neq \rho_0 \tag{2.28}$$

The exact ground-state energy functional $E_0(\rho)$ is minimized only when $\rho = \rho_0$.

$$E_0 = \min_{n \in \mathcal{N}} E_{\nu_0}[\rho] \tag{2.29}$$

since the D map relating the state's set Ψ to the density's set $\mathcal{N}$ does not depend on the potential $\hat{V_0}$ of the system.

2.4 Kohn-Sham Equations

In the Kohn-Sham ansatz the problem of a system of N interacting electrons in a static external potential is replaced by a system of N non-interacting electrons in an effective potential. The fulcral hypothesis of the KS method is that for each $\rho(\mathbf{r})$ of the ground state of the system of interacting electrons, there is a system of non-interacting electrons that has the same density in the ground state.

The ground state energy functional of a system of N electrons in an external potential $\nu(\mathbf{r})$ can be written as,

$$E_\nu\left[\rho\right] = \left\langle \Psi\left[\rho\right]\right| H \left|\Psi\left[\rho\right]\right\rangle = F_{HK}\left[\rho\right] + \int \rho(\mathbf{r})\nu(\mathbf{r})d\mathbf{r} + E_{nn} \tag{2.30}$$

where $F_{HK}[\rho]$ is a universal functional of the electron density. Searching for the ground state energy $E_0 = \min_{\{\rho\}} E_\nu\left[\rho\right]$ is done by solving the Euler-Lagrange equations,

$$\frac{\delta}{\delta\rho(\mathbf{r})}\left[E_\nu\left[\rho(\mathbf{r})\right] - \mu\left(\int \rho(\mathbf{r})d\mathbf{r} - N\right)\right] = \frac{\delta F_{HK}\left[\rho(\mathbf{r})\right]}{\delta\rho(\mathbf{r})} + \nu(\mathbf{r}) - \mu = 0 \tag{2.31}$$

where μ is a Lagrange multiplier imposing the conservation of the total number of electrons. The state of a system of N non-interacting electrons subject to an external potential $\nu_s(\mathbf{r})$ is the Slater determinant of the orbitals $\phi_i(\mathbf{r})$ that satisfy the equations,

$$\left[-\frac{1}{2}\nabla^2 + \nu_s(\mathbf{r})\right]\phi_i(\mathbf{r}) = \epsilon_i\phi_i(\mathbf{r}) \tag{2.32}$$

where the electron density is the sum of the square modulus of these orbitals,

$$\rho(\mathbf{r}) = \sum_{i=1}^{N} |\phi_i(\mathbf{r})|^2 \ . \tag{2.33}$$

The total energy of the system is given by,

$$E_{\nu_s}[\rho(\mathbf{r})] = T_s[\rho(\mathbf{r})] + \int \rho(\mathbf{r})\nu_s(\mathbf{r})d\mathbf{r} \ , \tag{2.34}$$

where the first term is the kinetic energy

$$T_s[\rho(\mathbf{r})] = -\frac{1}{2}\sum_{i=1}^{N}\int \phi_i^*(\mathbf{r})\nabla^2\phi_i(\mathbf{r})d(\mathbf{r}) \ . \tag{2.35}$$

The ground state energy can then be obtained by minimizing this energy with respect to the electron density.

$$\frac{\delta}{\delta\rho(\mathbf{r})}\left[E_{\nu_s}[\rho(\mathbf{r})] - \mu_s\left(\int \rho(\mathbf{r})d\mathbf{r} - N\right)\right] = \frac{\delta T_s[\rho(\mathbf{r})]}{\delta\rho(\mathbf{r})} + \nu_s(\mathbf{r}) - \mu_s = 0 \tag{2.36}$$

The functional $F_{HK}[\rho(\mathbf{r})]$ from before can then be rewritten as,

$$F_{HK}[\rho(\mathbf{r})] = T + V + W = T_s + V_{\text{Hartree}} + (T - T_s + V - V_{\text{Hartree}} + W) \tag{2.37}$$

$$V_{\text{Hartree}} = \frac{1}{2}\int \frac{\rho(\mathbf{r_1})\rho(\mathbf{r_2})}{|\mathbf{r_1} - \mathbf{r_2}|}d\mathbf{r_1}d\mathbf{r_2} \tag{2.38}$$

$$F_{HK}[\rho(\mathbf{r})] = T_s[\rho(\mathbf{r})] + \frac{1}{2}\int \frac{\rho(\mathbf{r_1})\rho(\mathbf{r_2})}{|\mathbf{r_1} - \mathbf{r_2}|}d\mathbf{r_1}d\mathbf{r_2} + E_{xc}[\rho(\mathbf{r})] \tag{2.39}$$

calling the unknown terms in the parenthesis the exchange-correlation energy functional $E_{xc}[\rho(\mathbf{r})]$. This term accounts for the remaining energy. It cannot be derived and must be approximated, the simplest of these approximations was proposed in [8], is the local density approximation (LDA). From this exchange-correlation energy functional, the exchange-correlation potential is defined as

$$\nu_{xc}([\rho(\mathbf{r})]\,;\mathbf{r}) = \frac{\delta E_{xc}[\rho(\mathbf{r})]}{\delta\rho(\mathbf{r})}\ . \tag{2.40}$$

The Euler-Lagrange equations of a system of interacting electrons in an external potential $\nu(\mathbf{r})$ are rewritten as,

$$\frac{\delta}{\delta\rho(\mathbf{r})}\left[E_\nu\left[\rho(\mathbf{r})\right] - \mu\int\rho(\mathbf{r})d\mathbf{r}\right] = \frac{\delta T_s\left[\rho(\mathbf{r})\right]}{\delta\rho(\mathbf{r})} + \nu(\mathbf{r}) +$$

$$+\int\frac{\rho(\mathbf{r})}{|\mathbf{r}-\mathbf{r}'|}d\mathbf{r}' + \nu_{xc}([\rho(\mathbf{r})]\,;\mathbf{r}) - \mu = 0 \tag{2.41}$$

and our new effective potential for the independent electron system is defined

$$\nu_s(\mathbf{r}) = \nu(\mathbf{r}) + \int\frac{\rho(\mathbf{r})}{|\mathbf{r}-\mathbf{r}'|}d\mathbf{r}' + \nu_{xc}([\rho(\mathbf{r})]\,;\mathbf{r})\ . \tag{2.42}$$

The electron density of the original interacting system is then obtained from

$$\left[-\frac{1}{2}\nabla^2 + \nu(\mathbf{r}) + \int\frac{\rho(\mathbf{r})}{|\mathbf{r}-\mathbf{r}'|}d\mathbf{r}' + \nu_{xc}([\rho]\,;\mathbf{r})\right]\phi_i(\mathbf{r}) = \epsilon_i\phi_i(\mathbf{r}) \tag{2.43}$$

$$\rho = \sum_i |\phi_i|^2 \tag{2.44}$$

and the total energy of the original interacting system is obtained

$$E_{KS}\left[\rho(\mathbf{r})\right] = T_s\left[\rho(\mathbf{r})\right] + \int\rho(\mathbf{r})\nu(\mathbf{r})d\mathbf{r} +$$

$$+\frac{1}{2}\int\frac{\rho(\mathbf{r_1})\rho(\mathbf{r_2})}{|\mathbf{r_1}-\mathbf{r_2}|}d\mathbf{r_1}d\mathbf{r_2} + E_{xc}\left[\rho(\mathbf{r})\right] + E_{nn} \tag{2.45}$$

2.5 Exchange-Correlation Approximations

The form of the exchange correlation (xc) functional continues to be a hurdle for DFT. Nonetheless progress has been steady throughout the years. In 2001 John Perdew and Karla Schmidt published a paper [11] in which they describe a ladder, Jacob's ladder, where each rung represents a different family of xc approximations. These approximations are ordered vertically in ascending order of accuracy, and are: local spin density approximation; generalized gradient approximation; meta-generalized gradient approximation; exact exchange and compatible correlation and lastly exact exchange and exact partial correlation. This Jacob's ladder serves as a representation of the progress to be done in the pursuit of an ever more accurate xc approximation. In general each rung builds upon the previous one with more parameters. The last as of yet to be included rung on this ladder would be the perfect approximation, able to achieve "chemical accuracy" (1kcal/mol). In this brief overview we will stop at the second rung since that was what was used in this work.

2.5.1 Local Density Approximation

The first xc functional, the local density approximation (LDA), was introduced by Kohn and Sham in the same paper as the equations bearing their name [8]. This simple approximation treats the electron system locally as an homogeneous electron gas (HEG). This method is best applied to systems with slow-varying electron densities since that is the assumption made in the approximation. This exchange correlation energy is

$$E_{xc}^{\mathrm{LDA}}[\rho] = \int \rho(\mathbf{r})\epsilon_{xc}(\rho)d\mathbf{r} \tag{2.46}$$

where $\epsilon_{xc}(\rho)$ is the exchange and correlation energy per electron of a uniform electron gas with density ρ.

Like for all xc functionals, $\epsilon_{xc}(\rho)$ can be divided into an exchange contribution and a correlation contribution,

$$\epsilon_{xc}(\rho) = \epsilon_x(\rho) + \epsilon_c(\rho) \tag{2.47}$$

with the exchange contribution already determined by Dirac [12]. This contribution is as follows,

$$\epsilon_x(\rho) = -\frac{3}{4}\left(\frac{3}{\pi}\right)^{1/3}\rho^{1/3}(\mathbf{r}) \;\approx -0.7386\rho^{1/3}(\mathbf{r}) \tag{2.48}$$

The correlation contribution does not have such a clean form, nonetheless several parametrizations exist, which are fitted to accurate Monte-Carlo results [13]. An examples of this is [14]. This was done by fitting a complex function for the correlation energy to values obtained from quantum Monte Carlo simulations of a homogeneous electron gas (HEG).

2.5.2 Generalized Gradient Approximations

Generalized gradient approximations (GGA) make the exchange correlation energy dependent on the gradient of the electron density in addition to the density itself. This modification achieves more accurate total energies [15], atomization energies [15–17], energy barriers and structural energy differences [18, 19]. This approximation was first proposed by Ma and Brueckner [20] and considers a correlation energy that is given by,

$$\epsilon_{\mathrm{c}} = \int d^3 r \rho(r) \left[e_{\mathrm{c}}^{\mathrm{unif}}(\rho(r)) + \beta(\rho(r)) |\nabla \rho(r)|^2 + ... \right] \tag{2.49}$$

This β function that needs to be fitted is constructed from several considerations. Namely: in the slow-varying limit it is given by its second-order gradient expansion; in the fast-varying limit it reduces to the opposite of the LDA approximation.

PBE and PBEsol Approximation

In this work the approximation used for all the DFT calculations was the Perdew-Burke-Ernzerhof Functional for solids (PBESol) [21]. PBESol is a different parametrization on the PBE approximation, with both of them being generalized gradient approximations (GGA). In the original article for PBEsol [21] 18 solids were tested including semiconductors, ionic solids, simple and transition metals. The tests showed that out of LSDA, TPSS (meta-GGA), PBE, and PBEsol, PBEsol had the least absolute error in 3 ouf the 4 categories of solids. The exception were the ionic solids for which LSDA had the least mean error. For this reason PBEsol was chosen for this work.

2.6 Lattice Vibrations and Phonons

A crystal naturally has certain frequencies of motion at which it's constituents oscillate simultaneously in a periodic fashion, these are called the normal modes of the system. This is the classical interpretation of this microscopic phenomenon. In quantum mechanics this collective movement is called a phonon, a quasi-particle that represents the quantization of the normal modes.

Let's obtain these normal modes of a crystal system. The change in the energy of a system when small changes in the nuclear positions occur allows for the calculation of the vibrational properties of the system. Let's consider a system where an atom κ at a position $\mathbf{R}_\kappa$, in a unit cell a at a position $\mathbf{R}^a$, deviates from it's equilibrium position $\mathbf{R}_\kappa^a$ by a time-dependent amount $\mathbf{u}_\kappa^a(t)$

$$\mathbf{R}^a_\kappa(t) = \mathbf{R}^a_\kappa + \mathbf{u}^a_\kappa(t) = (\mathbf{R}^a + \mathbf{R}_\kappa) + \mathbf{u}^a_\kappa(t) \; . \tag{2.50}$$

Using a Taylor expansion we can write the energy of the system as a function of its derivatives with respect to this perturbation,

$$E\left(\{\mathbf{R}^\alpha_\kappa(t)\}\right) \approx E\left(\{\mathbf{R}^\alpha_\kappa\}\right) + \sum_{\alpha\kappa\alpha} \left(\frac{\partial E}{\partial \mathbf{u}^a_{\kappa\alpha}}\right) \mathbf{u}^a_{\kappa\alpha}(t) \tag{2.51}$$

$$+ \sum_{ak\alpha} \sum_{bk'\beta} \frac{1}{2} \left(\frac{\partial^2 E}{\partial \mathbf{u}^a_{\kappa\alpha} \mathbf{u}^b_{\kappa'\beta}}\right) \mathbf{u}^a_{\kappa\alpha} \mathbf{u}^b_{k'\beta} + \dots$$

Remembering that we consider the ions to be in their equilibrium position (i.e. in a local minimum of the energy surface), the first derivative of the energy with respect to these deviations is zero. Since $\mathbf{u}^2$ is small, $\mathbf{u}^3$ and other terms are considered to be negligible. This is collectively referred to as the Harmonic approximation:

$$E\left(\{\mathbf{R}^\alpha_\kappa(t)\}\right) \approx E\left(\{\mathbf{R}^\alpha_\kappa\}\right) + \sum_{a\kappa\alpha} \sum_{b\kappa'\beta} \frac{1}{2} \left(\frac{\partial^2 E}{\partial \mathbf{u}^a_{\kappa\alpha} \mathbf{u}^b_{\kappa'\beta}}\right) \mathbf{u}^a_{\kappa\alpha} \mathbf{u}^b_{\kappa'\beta} \tag{2.52}$$

The second derivatives of the energy form the interatomic force constant (IFC) matrix in real space:

$$C_{\kappa\alpha,\kappa'\beta}(a,b) = \left(\frac{\partial^2 E}{\partial \mathbf{u}^a_{\kappa\alpha} \mathbf{u}^b_{\kappa'\beta}}\right) \tag{2.53}$$

By the Bloch Theorem we can say that the absolute positions of cells a and b don't matter, only their relative distances matter so we can set one of them to 0 and another to $b - a$.

$$\frac{\partial^2 E}{\partial \mathbf{u}^a_{\kappa\alpha} \partial \mathbf{u}^b_{\kappa'\beta}} = \frac{\partial^2 E}{\partial \mathbf{u}^0_{\kappa\alpha} \partial \mathbf{u}^{b-a}_{\kappa'\beta}} \tag{2.54}$$

By the definition of force,

$$\mathbf{F}^a_\kappa = M_\kappa \mathbf{a}^a_\kappa = -\nabla_{\mathbf{R}^a_\kappa} E = -\frac{\partial E}{\partial \mathbf{u}^a_{\kappa\alpha}} \tag{2.55}$$

and the definition of acceleration,

$$\mathbf{a}^a_\kappa = \frac{\partial^2 \mathbf{R}^a_\kappa(t)}{dt^2} = \frac{\partial^2 \left(\mathbf{R}^a_\kappa + \mathbf{u}^a_\kappa(t)\right)}{\partial t^2} = \frac{\partial^2 \mathbf{u}^a_\kappa(t)}{\partial t^2} \tag{2.56}$$

equation (2.55) becomes,

$$-\frac{\partial E}{\partial \mathbf{u}^a_{\kappa\alpha}} = M_\kappa \frac{\partial^2 \mathbf{u}^a_{\kappa\alpha}}{\partial t^2} \tag{2.57}$$

After this step we can insert equation (2.52) into equation (2.57):

$$-\frac{\partial E}{\partial \mathbf{u}^a_{\kappa\alpha}} = -\sum_{b\kappa'\beta} \left(\frac{\partial^2 E}{\partial \mathbf{u}^a_{\kappa\alpha} \partial \mathbf{u}^b_{\kappa'\beta}} \right) \mathbf{u}^b_{\kappa'\beta} \tag{2.58}$$

$$M_\kappa \frac{\partial^2 \mathbf{u}^a_{\kappa\alpha}}{\partial t^2} = -\sum_{b\kappa'\beta} \left(\frac{\partial^2 E}{\partial \mathbf{u}^a_{\kappa\alpha} \partial \mathbf{u}^b_{\kappa'\beta}} \right) \mathbf{u}^b_{\kappa'\beta} \tag{2.59}$$

To find an ansatz we will remember that all displacements have the same temporal dependency of the form $e^{-i\omega_m t}$ and obeys the Bloch Theorem. A valid ansatz is then, in a normal mode,

$$\mathbf{u}^a_{\kappa\alpha}(t) = \eta_{m\mathbf{q}}(\kappa\alpha) e^{i\mathbf{q}\cdot\mathbf{R}_a} e^{-i\omega_{m\mathbf{q}} t} \; . \tag{2.60}$$

Where each displacement is characterized by a wave vector $\mathbf{q}$. Also, $\eta_{m\mathbf{q}}$ is the displacement along α. Taking the first and second time derivatives,

$$\frac{\partial \mathbf{u}^a_{\kappa\alpha}(t)}{\partial t} = (-i\omega_{m\mathbf{q}})\, \eta_{m\mathbf{q}}(\kappa\alpha) e^{i\mathbf{q}\cdot\mathbf{R}_a} e^{-i\omega_{m\mathbf{q}} t} \tag{2.61}$$

$$\frac{\partial^2 \mathbf{u}^a_{\kappa\alpha}(t)}{\partial t^2} = -\omega^2_{m\mathbf{q}} \eta_{m\mathbf{q}}(\kappa\alpha) e^{i\mathbf{q}\cdot\mathbf{R}_a} e^{-i\omega_{m\mathbf{q}} t} \tag{2.62}$$

and inserting them into equation (2.59) yields,

$$-M_\kappa \omega^2_{m\mathbf{q}} \eta_{m\mathbf{q}}(\kappa\alpha) e^{i\mathbf{q}\cdot\mathbf{R}_a} e^{-i\omega_{m\mathbf{q}} t} = -\sum_{b\kappa'\beta} \left(\frac{\partial^2 E}{\partial \mathbf{u}^a_{\kappa\alpha} \partial \mathbf{u}^b_{\kappa'\beta}} \right) \eta_{m\mathbf{q}}\left(\kappa'\beta\right) e^{i\mathbf{q}\cdot\mathbf{R}_b} e^{-i\omega_{m\mathbf{q}} t} \tag{2.63}$$

furthermore by multiplying both sides by $e^{i\omega_{m\mathbf{q}} t}$,

$$M_\kappa \omega^2_{m\mathbf{q}} \eta_{m\mathbf{q}}(\kappa\alpha) e^{i\mathbf{q}\cdot\mathbf{R}_a} = \sum_{b\kappa'\beta} \left(\frac{\partial^2 E}{\partial \mathbf{u}^a_{\kappa\alpha} \partial \mathbf{u}^b_{\kappa'\beta}} \right) \eta_{m\mathbf{q}}\left(\kappa'\beta\right) e^{i\mathbf{q}\cdot\mathbf{R}_b} \tag{2.64}$$

reordering the sums and multiplying both sides by $e^{-i\mathbf{q}\cdot\mathbf{R}_a}$ gives equation (2.65).

$$M_\kappa \omega^2_{m\mathbf{q}} \eta_{m\mathbf{q}}(\kappa\alpha) = \sum_{\kappa'\beta} \left[\sum_b \left(\frac{\partial^2 E}{\partial \mathbf{u}^a_{\kappa\alpha} \partial \mathbf{u}^b_{\kappa'\beta}} \right) e^{i\mathbf{q}\cdot(\mathbf{R}_b - \mathbf{R}_a)} \right] \eta_{m\mathbf{q}}\left(\kappa'\beta\right) \tag{2.65}$$

Let's use the IFC's from now on. Then, the previous equation takes the form,

$$M_\kappa \omega_{m\mathbf{q}}^2 \eta_{m\mathbf{q}}(\kappa\alpha) = \sum_{\kappa'\beta} \left[\sum_b C_{\kappa\alpha,\kappa'\beta}(a,b) e^{i\mathbf{q}\cdot(\mathbf{R}_b - \mathbf{R}_a)} \right] \eta_{m\mathbf{q}}(\kappa'\beta) \tag{2.66}$$

as we can see, the origin a does not matter anymore and we can set it to zero, since the IFC's depend only on the relative distances between the atoms.

$$M_\kappa \omega_{m\mathbf{q}}^2 \eta_{m\mathbf{q}}(\kappa\alpha) = \sum_{\kappa'\beta} \left[\sum_b C_{\kappa\alpha,\kappa'\beta}(0,b) e^{i\mathbf{q}\cdot\mathbf{R}_b} \right] \eta_{m\mathbf{q}}(\kappa'\beta) \tag{2.67}$$

The term in brackets in equation (2.67) is nothing else than the discrete Fourier transform of the interatomic force constant in real space:

$$\tilde{C}_{\kappa\alpha,\kappa'\beta}(\mathbf{q}) = \frac{1}{N} \sum_{a,b} C_{\kappa\alpha,\kappa'\beta}(a,b) e^{-i\mathbf{q}\cdot(\mathbf{R}_a - \mathbf{R}_b)} \tag{2.68}$$

$$= \sum_b C_{\kappa\alpha,\kappa'\beta}(0,b) e^{i\mathbf{q}\cdot\mathbf{R}_b} \tag{2.69}$$

Therefore, the movement of the atoms can be defined in terms of the dynamical equations,

$$M_\kappa \omega_{m\mathbf{q}}^2 \eta_{m\mathbf{q}}(\kappa\alpha) = \sum_{\kappa'\beta} \tilde{C}_{\kappa\alpha,\kappa'\beta}(\mathbf{q}) \eta_{m\mathbf{q}}(\kappa'\beta) \tag{2.70}$$

$$\frac{1}{\sqrt{M_\kappa}} \gamma_{m\mathbf{q}}(\kappa\alpha) = \eta_{m\mathbf{q}}(\kappa\alpha) \tag{2.71}$$

$$\mathbf{u}_{\kappa\alpha}^a(t) = \frac{1}{\sqrt{M_\kappa}} \gamma_{m\mathbf{q}}(\kappa\alpha) e^{i\mathbf{q}\cdot\mathbf{R}_a} e^{-i\omega_{m\mathbf{q}} t} \tag{2.72}$$

Redoing previous algebra,

$$M_\kappa \frac{d^2 \mathbf{u}_{\kappa\alpha}^a(t)}{dt^2} = -\omega_{m\mathbf{q}}^2 \frac{M_\kappa}{\sqrt{M_\kappa}} \gamma_{m\mathbf{q}}(\kappa\alpha) e^{i\mathbf{q}\cdot\mathbf{R}_a} e^{-i\omega_{m\mathbf{q}} t} \tag{2.73}$$

$$M_\kappa \frac{d^2 \mathbf{u}_{\kappa\alpha}^a(t)}{dt^2} = \sum_b \sum_{\kappa'\beta} C_{\kappa\alpha,\kappa'\beta}(a,b) \eta_{m\mathbf{q}}(\kappa'\beta) e^{i\mathbf{q}\cdot\mathbf{R}_a} e^{-i\omega_{m\mathbf{q}} t} \tag{2.74}$$

$$\omega_{m\mathbf{q}}^2 \gamma_{m\mathbf{q}}(\kappa\alpha) \sqrt{M_\kappa} = \sum_{\kappa'\beta} \tilde{C}_{\kappa\alpha,\kappa'\beta}(\mathbf{q}) \frac{1}{\sqrt{M_{\kappa'}}} \gamma_{m\mathbf{q}}(\kappa'\beta) \tag{2.75}$$

$$\omega^2_{m\mathbf{q}}\gamma_{m\mathbf{q}}(\kappa\alpha) = \sum_{\kappa'\beta} \frac{\tilde{C}_{\kappa\alpha,\kappa'\beta}(\mathbf{q})}{\sqrt{M_\kappa M_{\kappa'}}}\gamma_{m\mathbf{q}}\,(\kappa'\beta) \tag{2.76}$$

Now we define the dynamical matrix as,

$$\tilde{D}_{\kappa\alpha,\kappa'\beta}(\mathbf{q}) = \frac{1}{\sqrt{M_\kappa M_{\kappa'}}}\tilde{C}_{\kappa\alpha,\kappa'\beta}(\mathbf{q}) \tag{2.77}$$

so finally the dynamical equation reduces to,

$$\sum_{\kappa'\beta} \tilde{D}_{\kappa\alpha,\kappa'\beta}(\mathbf{q})\gamma_{m\mathbf{q}}\,(\kappa'\beta) = \omega^2_{m\mathbf{q}}\gamma_{m\mathbf{q}}(\kappa\alpha) \tag{2.78}$$

This is an eigenvalue equation and can be solved by setting,

$$\det\left|\frac{1}{\sqrt{M_i M_j}}\tilde{C}^{\alpha\beta}_{ij}(\mathbf{q}) - \omega^2(\mathbf{q})\right| = 0 \tag{2.79}$$

which allows us to obtain the normal modes of vibration (the periodic movement of the system at a set frequency) as understood in classical mechanics.

2.7 Superconductivity

Superconductivity was discovered in 1911 by Heike Kamerlingh Onnes [1] when upon cooling a sample of mercury below 4.20K, it was observed that its electrical resistance collapsed from 0.11 Ω to 10^{-5} Ω. This research along with the synthesis of liquid helium won Onnes the 1913 Noble prize in physics. A graph from Onnes' research notes showing the observed superconducting phase transition can be seen in Figure 2.1. In the years following this discovery of superconductivity in mercury many more elements were found to also be superconducting. Research in the 1950's lead scientists to the discovery of many niobium based superconductors such as Nb_3Sn [22] and NbTi [23] still used today. In the 1980's a new class of superconducting materials emerged, known as the cuprates. These are unconventional (their superconducting mechanism cannot be described in terms of electron-phonon interactions) superconductors formed by layers of copper oxide and layers of other elements. Many materials in this class exhibit very high transition temperatures, some even with T_c's above 100K. The discovery of LBCO in 1986 [24] won Georg Bednorz and Karl Alex Müller the 1987 Nobel prize in Physics. In the last few decades a new hotly researched class of superconductors is the high-pressure hydrides, materials with a lot of hydrogen that have very high transition temperatures at very high pressures (in the order of GPa). Superconductivity is a phase transition and is classified in different ways: conventional or unconventional, type I or type II, etc. In type I superconductors a magnetic field is completely repelled by the Meissner effect. In type II superconductors the same field creates magnetic field vortices allowing the phenomenon known as flux pinning where the field lines are fixed. Superconductors are used nowadays as powerful electromagnets in magnetic resonance imaging machines as well as beam steering devices in particle accelerators.

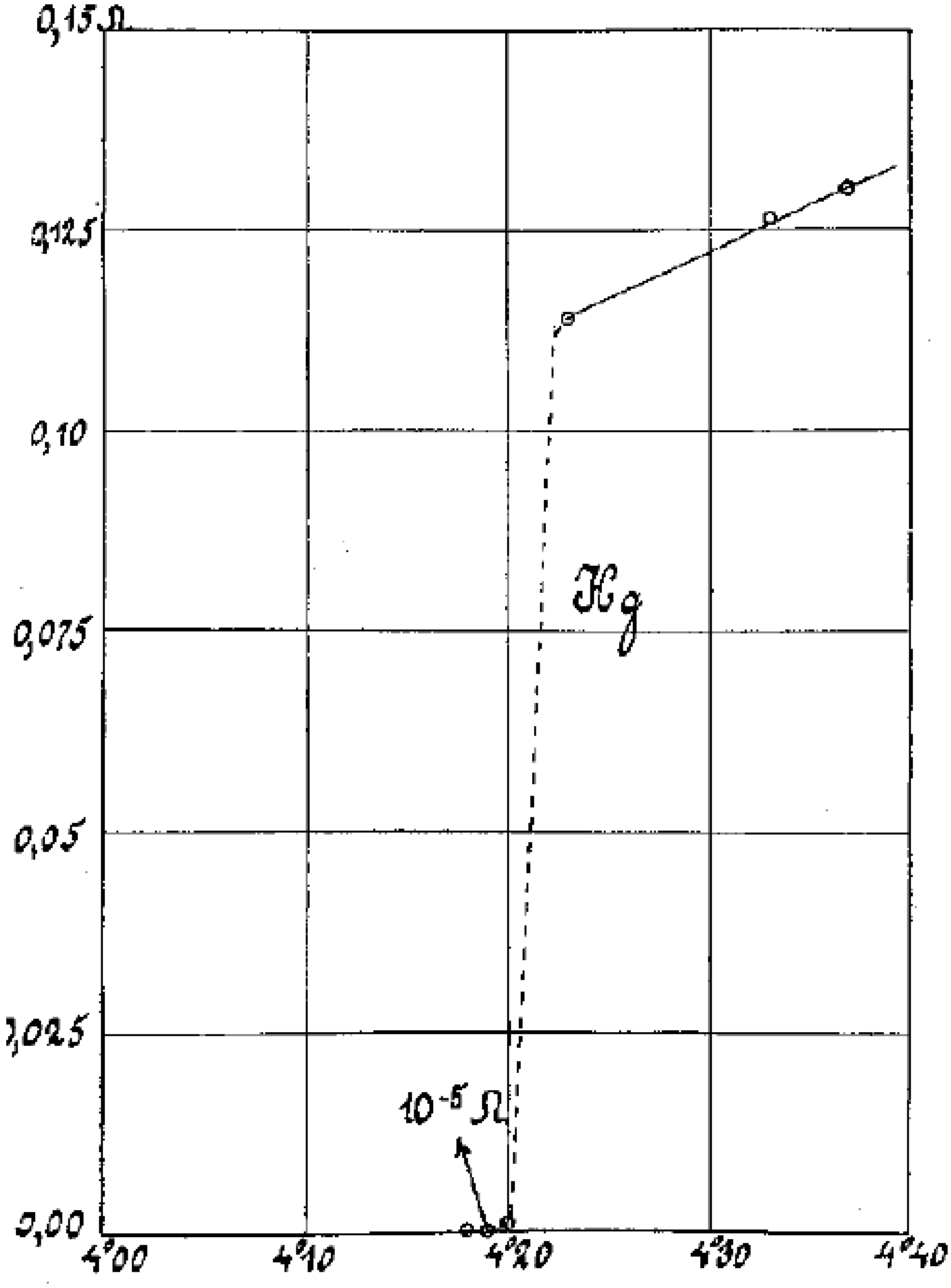

Figure 2.1: Resistance plot as a function of temperature of a mercury sample cooled with liquid helium. Plot taken from [1].

2.7.1 Bardeen-Cooper-Schrieffer Theory

In 1957 J. Bardeen, L. N. Cooper and J. R. Schrieffer published a paper on a novel microscopic description of superconductivity [25], that became known as BCS theory. This established a new model to describe the phenomenon and its mechanism. It also won them the 1972 Nobel Prize in Physics.

BCS theory is a way of describing superconductivity where electrons couple as Cooper pairs consisting of two electrons with an attractive interaction in a lattice by way of phonon mediation between them. This Cooper pair behaves as a boson when the electrons in the pair have opposite spin and momentum.

In a crystal the interaction between electrons with wave vectors κ and κ' and energies ϵ_κ and $\epsilon_{\kappa'}$, respectively, suffers a correction when ion displacements are considered, going from [26]

$$V^{\text{eff}}_{k,k'}(k,k') = \frac{4\pi}{|k-k'|^2} \tag{2.80}$$

to

$$V^{\text{eff}}_{k,k'}(k,k') = \frac{4\pi}{|k-k'|^2+k_0^2}\left(\frac{\omega^2}{\omega^2-\omega_q^2}\right) . \tag{2.81}$$

With k_0 being the Thomas-Fermi wave vector, $\omega = |\epsilon_\kappa - \epsilon_{\kappa'}|/\hbar$, $q = k - k'$ and ω_q being the frequency of a phonon with wave vector q. If the energy difference $\hbar\omega$ between the two electron states is less than the phonon energy $\hbar\omega_q$ an attractive interaction occurs.

The most impressive feat of this model is that it arrives at an expression for the critical transition temperature [25]:

$$T_\text{c} = 1.13\,\omega_\text{D} \exp\left(\frac{-1}{N(E_\text{F})V}\right) . \tag{2.82}$$

Where ω_D is the Debye frequency, $N(E_F)$ is the occupancy at the Fermi level and V is the effective coupling.

A full derivation of BCS and/or Migdal-Eliashberg theory will not be included in this thesis. A full derivation of the T_c function from BCS theory is shown in [27] and one for the Migdal-Eliashberg T_c function is available at [28].

2.7.2 Migdal-Eliashberg Theory

The history of Migdal-Eliashberg theory is rather long, the model itself being tweaked throughout the years. The initial Eliashberg theory [29] was presented in 1960 and was tweaked in the following years by physicists such as Morel and Anderson [30] and Mcmillan and Dynes [31, 32].

Migdal-Eliashberg theory takes into account considerations that were left out of the BCS formalism. For instance the electron-ion interactions are no longer considered to be instantaneous. The key quantity in this theory is the spectral function $\alpha^2F(\omega)$ defined in equation (2.83) as a sum of the phonons frequencies and coupling constants of mode ν and wave vector $q = k - k'$ which gives the electron-phonon interaction the form of a spectral density.

$$\alpha^2F(\omega) = \sum_{q\nu} \omega_{q\nu}\lambda_{q\nu}\delta(\omega - \omega_{q\nu}) \tag{2.83}$$

where $\lambda_{q\nu}$ is the electron-phonon coupling constant for mode ν at wave vector q and $\omega_{q\nu}$ the frequency for mode ν at wave vector q. Integrating this function for all frequencies gives the total coupling constant λ:

$$\lambda = 2\int \frac{\alpha^2F(\omega)}{\omega} d\omega = \sum_{qj} \lambda_{qj} w(q) \; . \tag{2.84}$$

Migdal-Eliashberg theory, after many approximations, arrives at a similar function for the critical transition temperature as BCS:

$$T_c = 1.13\,\omega_D\ \exp\left(-\frac{1+\lambda}{\lambda - \mu_c^*}\right) \; . \tag{2.85}$$

With a new parameter μ_c^*, the pseudo-Coulomb potential, that accounts for the Coulomb interaction screening. McMillan [31] updated this formula with the use of experimental data to,

$$T_\mathrm{c} = \frac{\omega_\mathrm{D}}{1.45} \exp\left(-\frac{1.04(1+\lambda)}{\lambda - \mu_c^*(1+0.62\lambda)}\right) \tag{2.86}$$

where ω_D is the same as in the BCS model. Dynes [32] further enhanced using even more data for a better fit and a different frequency average. Leading to,

$$T_\mathrm{c} = \frac{\omega_\mathrm{log}}{1.2} \exp\left(-\frac{1.04(1+\lambda)}{\lambda - \mu_c^*(1+0.62\lambda)}\right) \tag{2.87}$$

where the term ω_log is the logarithmic average frequency.

$$\omega_{\log} = \exp\left[\frac{2}{\lambda}\int \frac{\alpha^2 F(\omega)}{\omega}\log(\omega)d\omega\right] \tag{2.88}$$

Chapter 3

2D Materials

3.1 Introduction

Single- and Few-layer or 2D materials are compounds formed by an arrangement of atoms in the shape of a flat surface. The unit cells of the crystal repeat in the x and y directions but not in the z direction.

As mentioned in the motivation, the groundbreaking discoveries of the early 2000's relating to this class of materials led the way for a new wave of research into and synthesis of new 2D materials. Many such materials have very remarkable characteristics [33], the semimetal graphene for instance has been reported to serve as a metallic field-effect transistor [2] and have very high thermal conductivity [34] as well as tensile strength [35]. At very low temperatures and magic angle conditions, the twisted bilayer arrangement of graphene presents many different phases such as a conductor, a superconductor and a Mott insulator as shown in [36]. Molybdenum disulfide in its 3D arrangement is heavily used in industry, as a lubricant, but in it's monolayer configuration it has been studied as a possible field-effect transistor, photodetector and solar cell due to being a high gap semiconductor [37].

As also mentioned in the motivation, the recent proliferation of large databases containing the structures and approximate properties of many compounds in this material class call for a high-throughput mechanism of studying them in detail. Particularly studies like [38] aim at screening large databases of 2D materials for promising superconductors. After a wide search, the highest T_c materials are further studied with tighter convergence criteria.

2D materials come in a variety of shapes and sizes, Figures 3.1 to 3.7 show structures of the most well known of these materials as shown in [33].

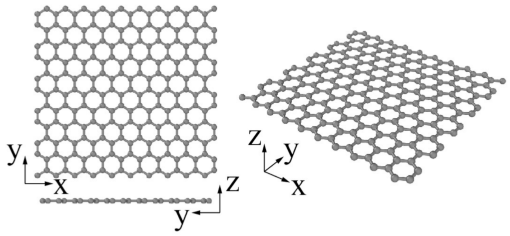

Figure 3.1: C (Graphene).

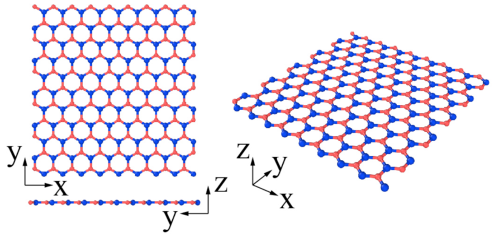

Figure 3.2: h-BN (Hexagonal Boron Nitride).

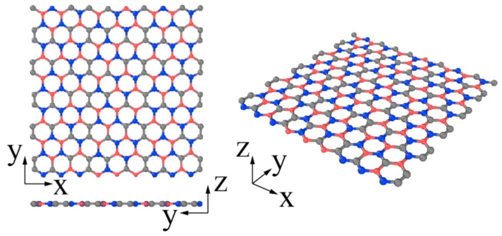

Figure 3.3: CBN (Boron Carbon Nitride).

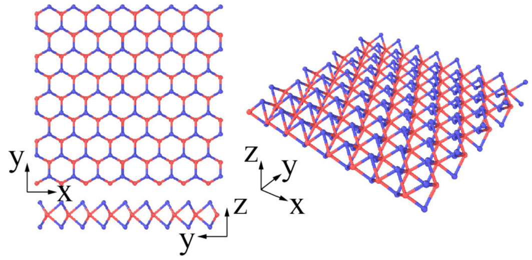

Figure 3.4: MoS_2 (Molybdenum Disulfide).

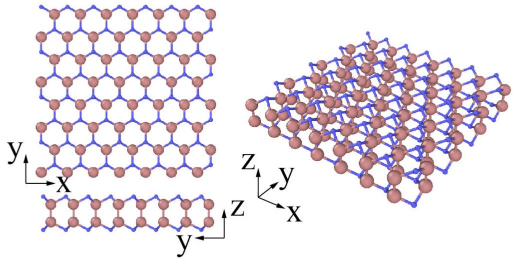

Figure 3.5: GaAs (Gallium Arsenide).

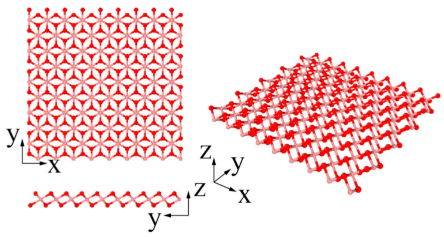

Figure 3.6: MnO_2 (Manganese Dioxide).

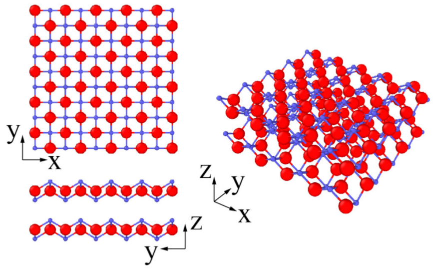

Figure 3.7: PbO (Lead Oxide).

3.2 Special considerations for a 2D system

Special considerations have to be made when doing DFT calculations on such materials. Planw-wave codes typically assume that the unit cell will infinitely repeat in all three directions. This causes a problem since 2D materials do not infinitely repeat in the z direction. To overcome this problem the height of the unit cell is increased until the interaction between the layers is minimized. Quantum Espresso implements a special module to treat 2D systems based on a truncated Coulomb interaction [39], allowing for a smaller cell and less plane waves than what would be needed otherwise. This ensures that the properties obtained by considering the system as an infinite 3D object are analogous to those of a 2D compound.

3.3 Phonons in 2D Structures

The phonon modes are divided into two different categories: acoustic and optical, each of which can also have either a longitudinal or a transverse motion. The four cases arising from these combinations are then: Longitudinal Acoustic (LA) and Optical (LO) as well as Transverse Acoustic (TA) and Optical (TO). Acoustic bands are the 3 bands that always start at a frequency of zero at Γ. Experimentally these phonons can be measured with techniques such as Raman Spectroscopy. One important effect to consider when viewing phonon spectrum plots is the LO-TO splitting in ionic crystals. The LO phonons are associated with long range Coulomb interactions of dipoles caused by the ion displacements. This does not occur in 2D materials as shown in [40].

Also, sometimes a material composed of very light and very heavy elements, (such as one studied in this work and shown below), has a frequency gap in its phonon dispersion plot. This frequency gap will exist between the low-frequency modes associated with the heavy atoms and the high-frequency modes associated with the light atoms. Phonon dispersion curves of 2D materials are slightly different than 3D ones. For 3D materials the 3 acoustic bands have a linear relation with the k-path near Γ. However, for 2D materials the flexural acoustic mode (ZA) of the z direction has a quadratic dependence with the momentum [41] [42]. We can see this difference by comparing a 3D case shown in Figure 3.8 with a 2D case shown in Figure 3.9.

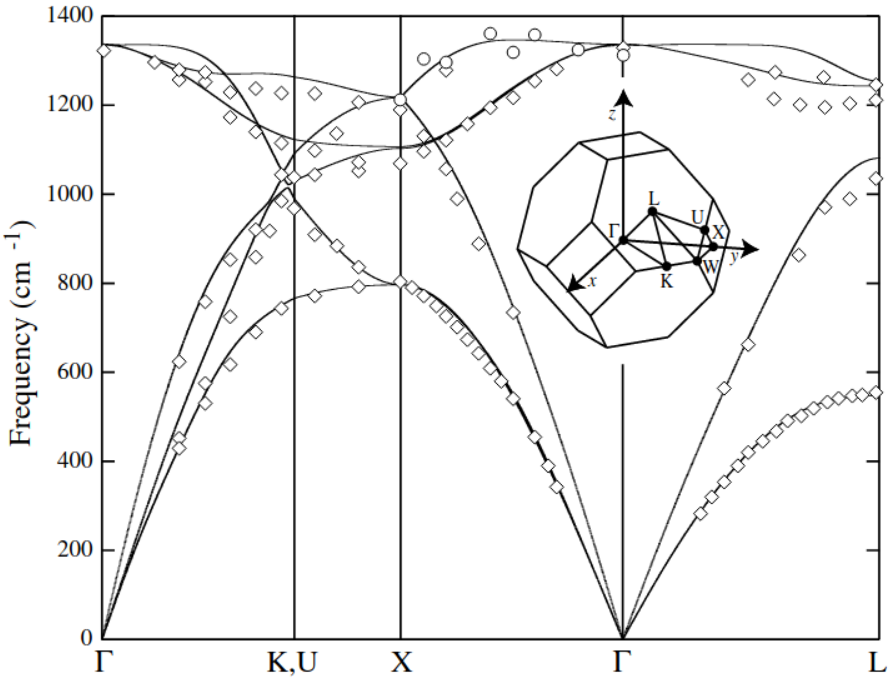

Figure 3.8: Diamond phonon spectrum taken from [43].

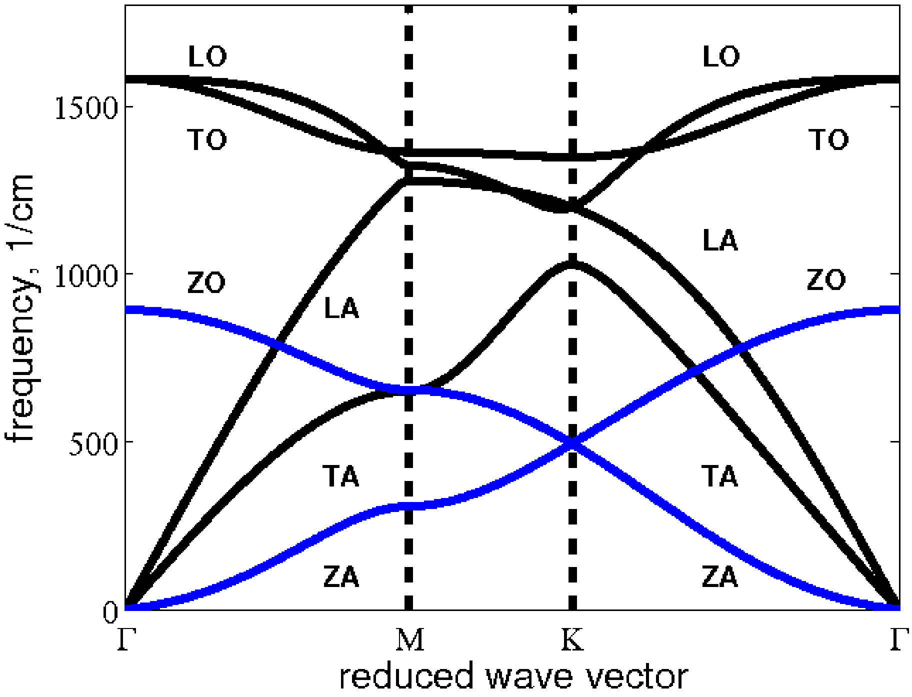

Figure 3.9: Graphene phonon spectrum taken from [44].

Chapter 4

Methodology and Test Cases

4.1 Methodology

To study the potential of single-layer materials as conventional superconductors, DFT calculations with tightened convergence parameters are necessary. Firstly to arrive at a relaxed geometry suitable for the chosen program and xc-functional, grid, etc. Secondly to perform the necessary electron-phonon calculations to obtain λ and $\omega_{\log}$ necessary to estimate the compound's critical transition temperature $\mathrm{T_c}$ following the McMillan-Dynes formula of the Migdal-Eliashberg formalism. Presented here is a study on the method of doing this by using the DFT code Quantum Espresso [45] and a study of the optimal parameters to obtain fast but reliable calculations of the materials phonon bands and expected transition temperatures.

In this section the objective is to test the different steps required to calculate the superconducting critical temperature. We will be using as test targets 2 well known systems, Nb_3Sn and B_2C. All calculations done in this thesis were made with the PBEsol [21] approximation to the xc-functional, and using the norm-conserving, scalar relativistic pseudo-potentials from PseudoDojo [46].

In order to obtain the superconducting transition temperature the following steps are necessary:

- Optimize the atomic positions and the lattice vectors of the material at study;
- Calculate the electron-phonon coefficients and obtain the electron-phonon mass enhancement parameter (λ) and the average phonon frequency ($\omega_{\log}$). We do this by using a double grid method;

- From these, we can obtain the superconducting critical temperature, T_c, using the McMillan formula 2.87.

4.2 Test case for Nb_3Sn

We start by performing calculations on Nb_3Sn, one of the most important superconductors for technological applications. It is a widely studied material, which offers a direct reference to validate our results. For this material, we will be calculating its band structure, electronic density of states, and phonon spectrum.

This compound has a simple cubic crystal lattice with space group $Pm\bar{3}n$ and 8 atoms in the unit cell, 6 Niobium and 2 Tin atoms. The Brillouin zone and unit cell are shown in Figure 4.1 and 4.2 respectively.

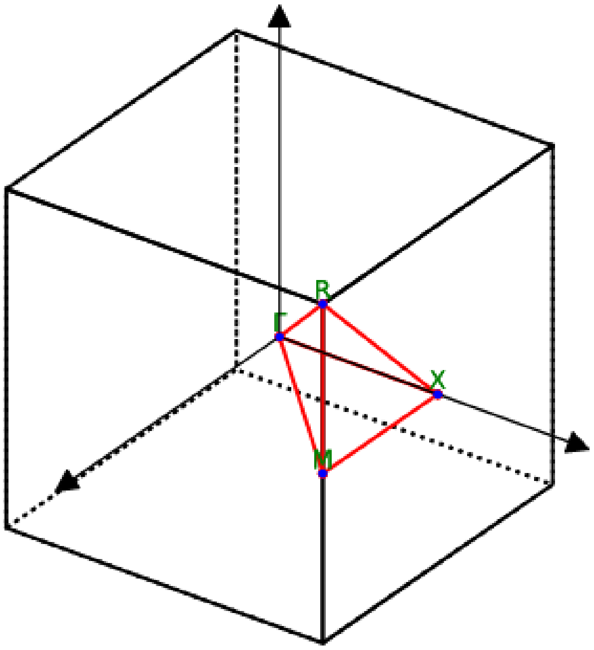

Figure 4.1: Nb_3Sn Brillouin zone with high-symmetry points highlighted as shown by ASE [47] documentation for Brillouin zone sampling.

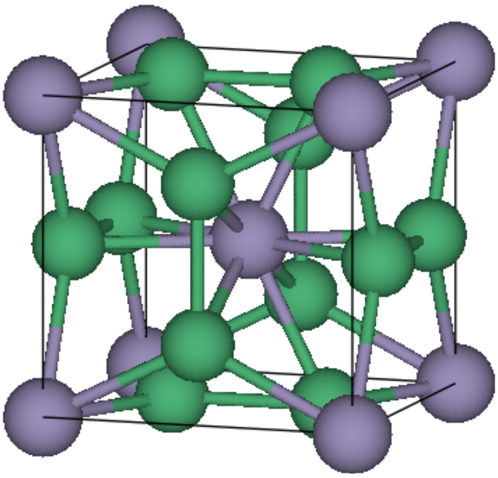

Figure 4.2: Nb_3Sn Structure visualized with the program VESTA [48]. Niobium atoms are in green and Tin atoms in grey.

We converged the k-grids and the energy cutoffs with respect to the total energy. We considered that the values were converged when the differences in total energy per atom were below 1 meV/atom. With the converged parameters, we optimized the geometry and lattice vectors and calculate the band structure (BS) and density of states (DOS), as shown in Figure 4.3.

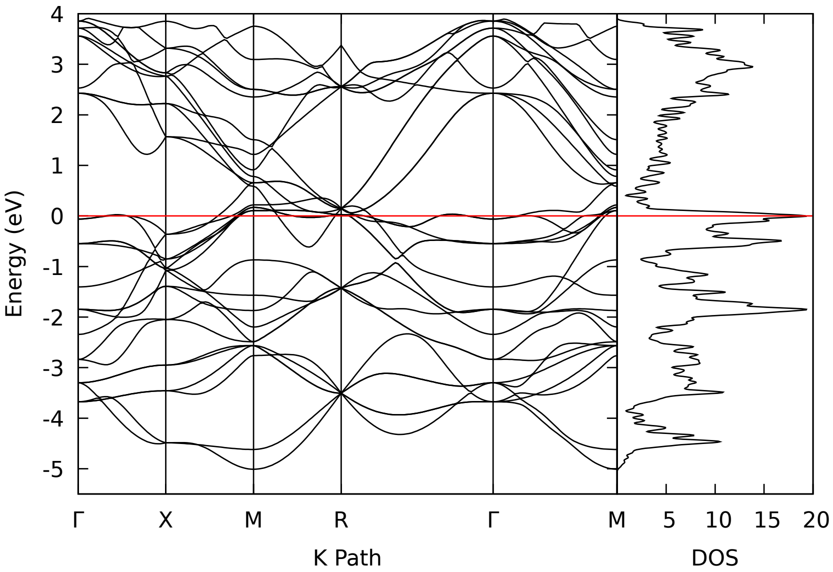

Figure 4.3: Nb_3Sn band structure and DOS (states/Ry).

This band structure and DOS are very similar to what is seen in the literature for example in [49] and in the Materials Project [50]. After this step, we calculated the phonon dispersion curves, which are shown in Figure 4.4.

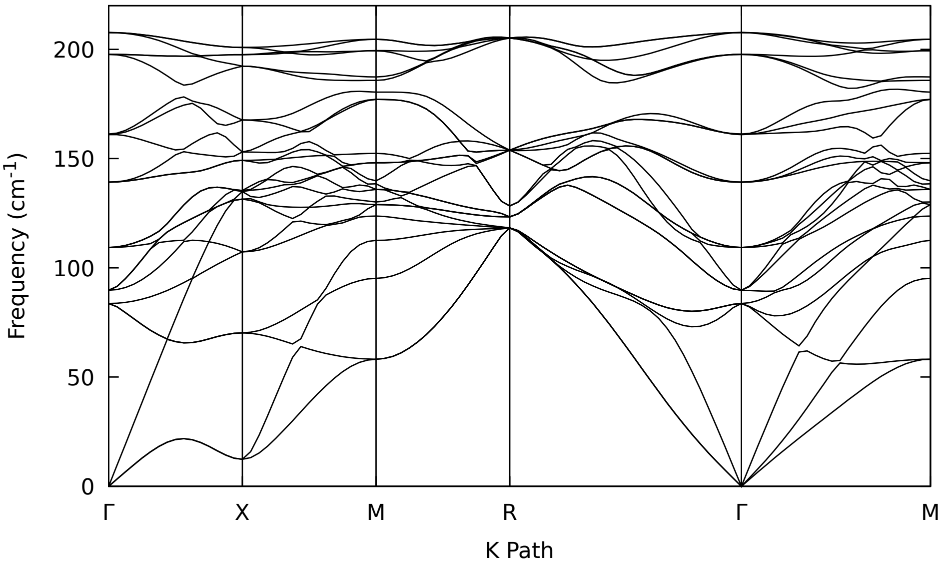

Figure 4.4: Nb_3Sn phonon spectra.

This is also very similar to what is seen in the literature for example in [51]. With this step completed a similar run on a 2D system was performed.

4.3 Test case for B_2C

To apply this same method for a 2D case, the material B_2C presented in a 2012 paper by Dai *et al.* [52] was chosen. It was then attempted to replicate the results of this paper. The material has a simple orthorhombic lattice with 2 boron and 1 carbon atoms in the unit cell. The structure of this material is shown in Figure 4.6.

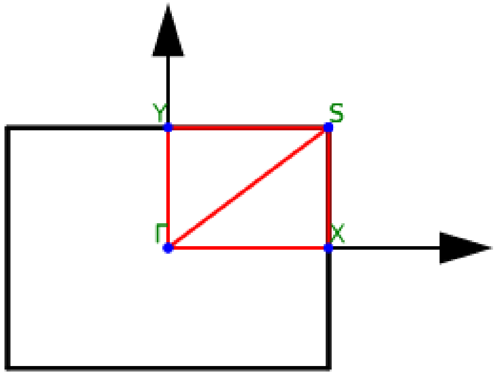

Figure 4.5: B_2C Brillouin zone with the high-symmetry points highlighted.

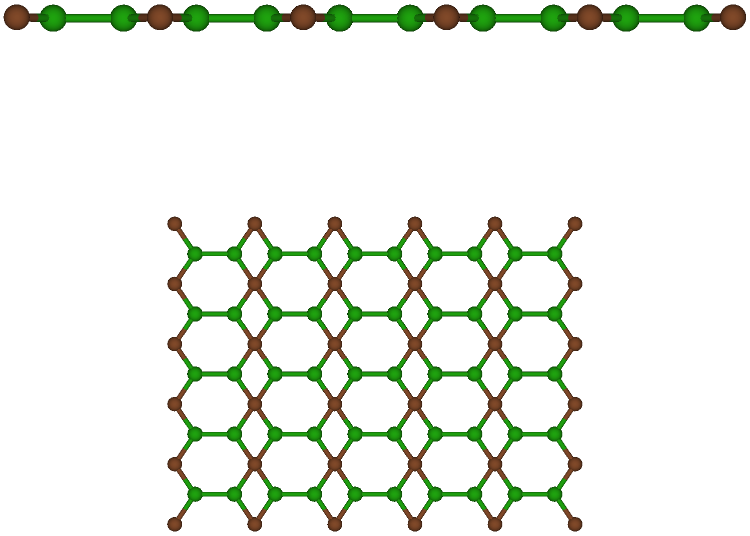

Figure 4.6: B_2C structure viewed from x (top panel) and z (bottom panel) direction. Boron atoms are shown in green whereas carbon atoms are shown in brown.

The geometry optimization step yielded the same structure as the reported one with a variation in the very small buckling. This buckling of the atoms is very sensitive to the parameters used and depending on what is used there may be no buckling at all. The obtained buckling was approximately 0.02 Å, less than the 0.032 Å reported in [52].

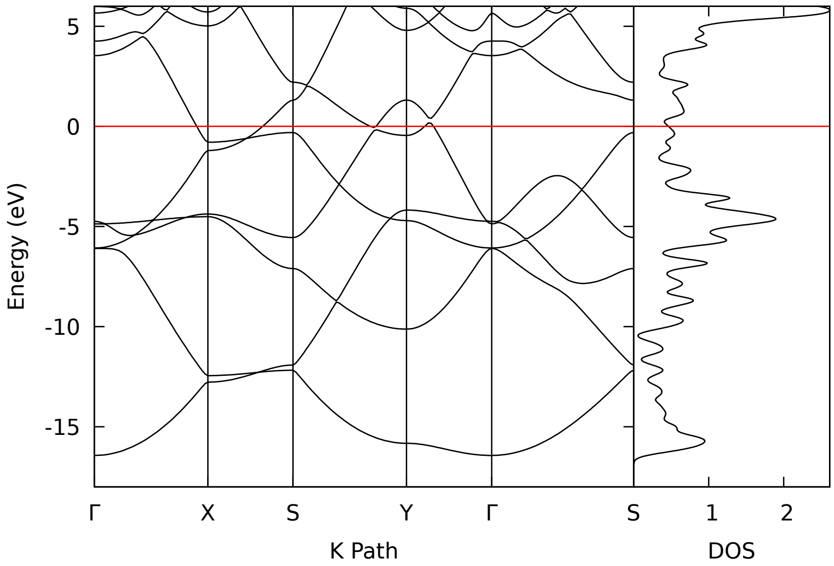

Figure 4.7: B_2C band structure and DOS (states/Ry).

The band structure and density of states obtained are again similar to the ones in [52]. The final step is to calculate the phonon dispersion curves and calculate the electron-phonon coefficients to obtain λ and $\omega_{\log}$ parameters, which we then use to estimate the superconducting critical transition temperature.

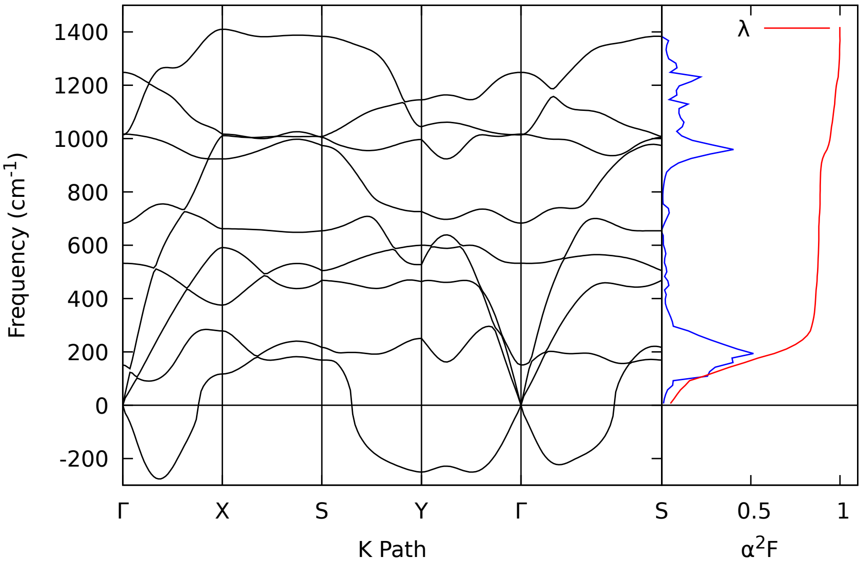

Figure 4.8: B_2C phonon spectra. The Eliashberg function α^2F is shown in blue and $\lambda(\omega)$ in red.

As is clear from the phonon plot in Figure 4.8 there are imaginary phonon modes present. Multiple runs were performed with different k-grids, different smearing functions and smearing values for the smearing function and different pseudopotential. However, all of them had these acoustic bands that dip significantly below zero. We note that this is in contradiction with the results from [52], where the material was found to be dynamically stable, even if a very soft phonon branch can already be seen. However, those results were obtained with extremely dense k-points grids, which we did not try due to the computational cost. The reason for this happening remains unclear, but these results seem to indicate that the material may be close to a dynamical instability in the conditions considered (zero pressure).

With these imaginary frequencies, the calculated electron-phonon coefficients are probably unreliable. Nonetheless, for the sake of completeness, we calculated λ and $\omega_{\log}$ considering only positive frequencies, and obtained $\lambda = 1.02$ and $\omega_{\log} = 268.4$ K, which compares to 0.92 and 314.8, respectively, from [52]. The obtained $T_c = 19.2$ K is, coincidentally, the same as in [52] (considering the same $\mu_c^* = 0.1$). The fact that the values obtained *ignoring* the negative frequencies are close to the results from [52] suggests that this phonon branch may not couple strongly to the electrons and, therefore, does not contribute significantly to λ.

4.4 Summary

In this Chapter, we tested and validated the workflow needed to calculate the superconducting critical temperature against two well known materials. Our results are, for the most part, in good agreement with the reported literature. The only exception is the presence of an imaginary phonon mode in B_2C, not documented in the literature. This was present regardless of the multiple calculation parameters tested.

With respect to the energy cutoff, we verified that the obtained converged values shown in Figures 4.9 and 4.10 were on top of the recommended values from PseudoDojo [46], indicating that those values can be safely used without further convergence tests.

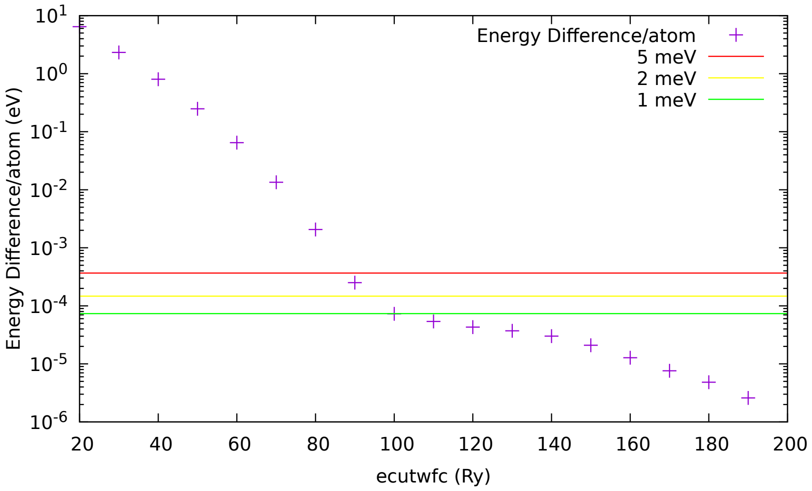

Figure 4.9: Nb_3Sn energy cutoff convergence test.

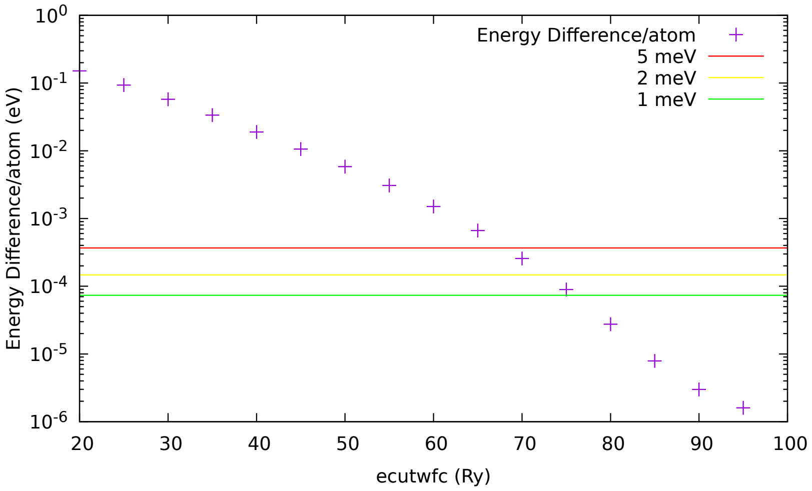

Figure 4.10: B_2C energy cutoff convergence test.

Chapter 5

Results

5.1 Materials

In this work, we selected five different materials from the 2D materials database of [5]. These were chosen from among the most symmetric, with largest density of states at the Fermi level, and fewest atoms of the materials in the database. This choice saved computing time while still allowing diverse materials to be selected. Furthermore the decision to study materials with a high occupancy at the Fermi level was deliberate to increase the chances of finding materials with higher transition temperatures (see equation 2.82).

As previously mentioned, the 2D nature of these materials requires a large inter-layer distance. Therefore the c vector of each unit cell was set to values ~ 18 Å. Of these five materials three were binary (H_2Pd, Tl_2Pb and NiS) and two were ternary (TiTeS and $CuAgTe_2$). Of these five materials, three have three atoms in the unit cell (H_2Pd, Tl_2Pb and TiTeS) and two have four atoms in the unit cell (NiS and $CuAgTe_2$). To study these materials' potential as superconductors the same methodology as in the test cases of B_2C and Nb_3Sn was performed.

However, as the goal is to automatize the workflow for hundreds of materials, we can't simply select the k- and q-grids by hand. As such, we used the function from PYMATGEN [53] to automatically define the initial k-grid for a given k-points per reciprocal atom density (kppa). This kppa measure was used so as to have a comparison to the 3D case. In order to converge this quantity we ran the same calculation for different kppa values, namely 500, 1000, 1500 and 3000. The grids were subsequently rounded up to even values in the k_x and k_y directions. We doubled the k-grid for the fine self-consistent field (scf) calculation, and used half for the q-point grid.

The energy cutoff for the wavefunctions was set to the maximum of PseudoDojo's [46] high precision hint of the elements in a given material. The values used were 98, 114, 100, 116 and 120 (in Ry) for H_2Pd, TiTeS, Tl_2Pb, NiS and $CuAgTe_2$ respectively. For each material, we used the high-symmetry path recommendation from the ASE documentation "Brillouin zone sampling" [47].

5.2 H_2Pd

The material H_2Pd crystallizes in a monoclinic cell, as shown in Figure 5.1. Lattice vectors a and b have equal length (2.82 Å) and form an angle of 60º. Its structure is shown in Figure 5.3 where the pink atoms are the elements of hydrogen and the gray atoms represent palladium. The hydrogen atoms lay 0.81 Å above and below the palladium atoms. These hydrogen atoms orient themselves around the palladium atoms in triangles offset by an angle of 60º so that when seen from above a hexagonal pattern forms.

Lastly, the obtained phonon dispersion curves for the different choice of k-point densities is shown in Figure 5.5. We also show the Eliashberg spectral function and λ for the 3000 kppa case.

The results for the different values of λ, $\omega_{\log}$ and consequently T_c, for different k-grids of this and all other materials discussed are shown in Table 1.

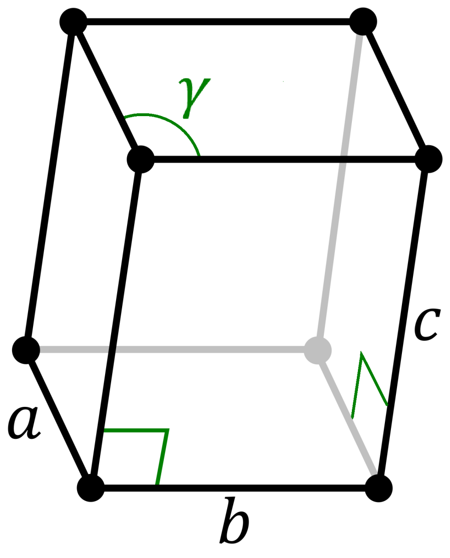

Figure 5.1: Monoclinic crystal system unit cell.

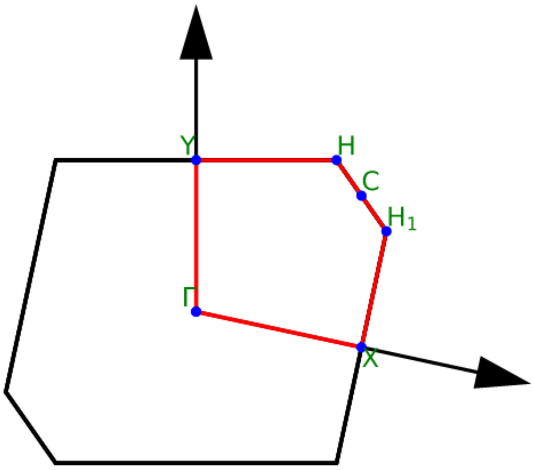

Figure 5.2: H_2Pd Brillouin zone with the path along high-symmetry points highlighted.

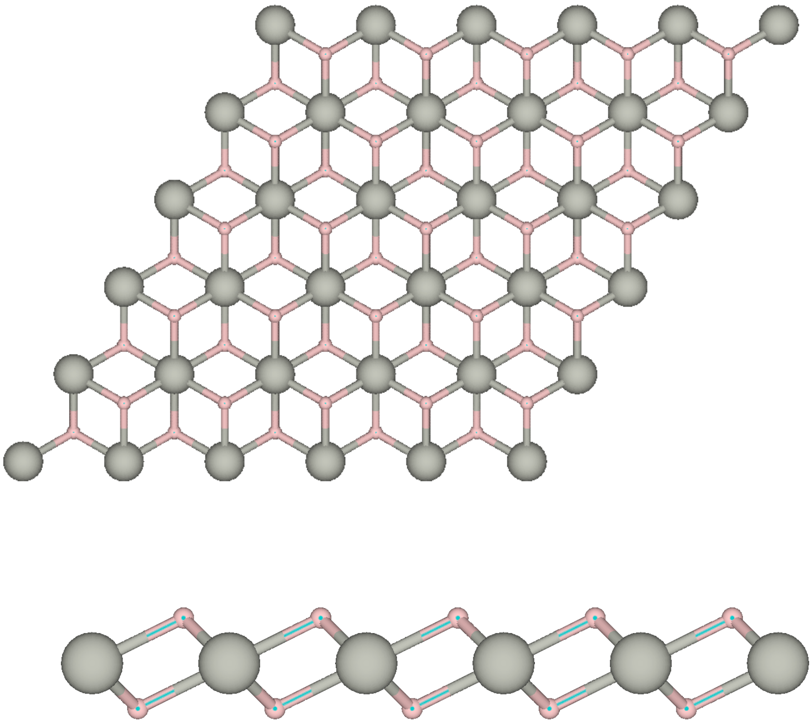

Figure 5.3: H_2Pd material visualized from the z (top panel) and x (bottom panel) directions respectively.

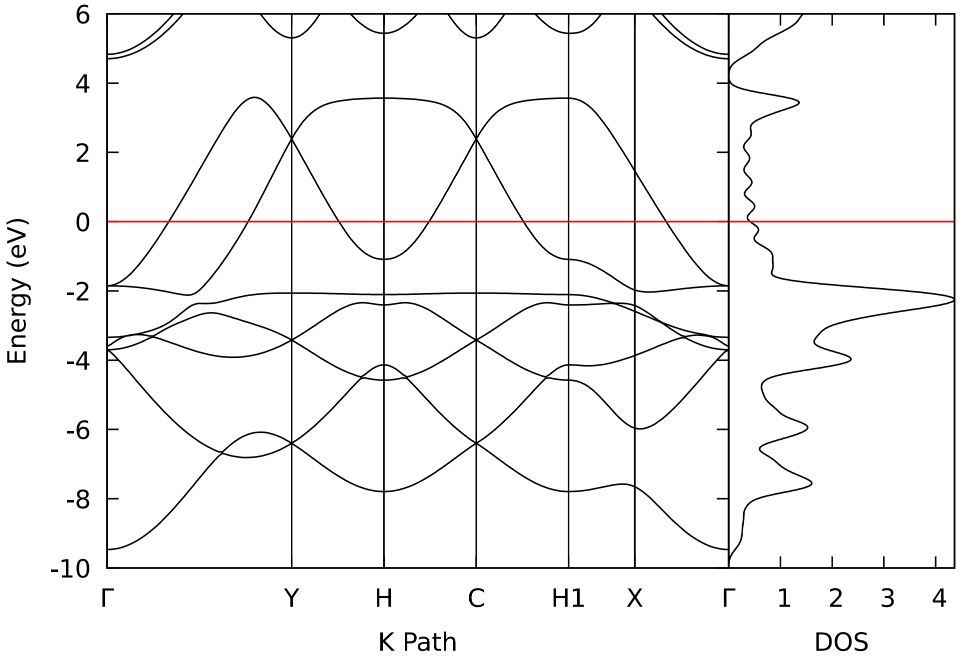

Figure 5.4: Electronic band structure and density of states (DOS) of H_2Pd.

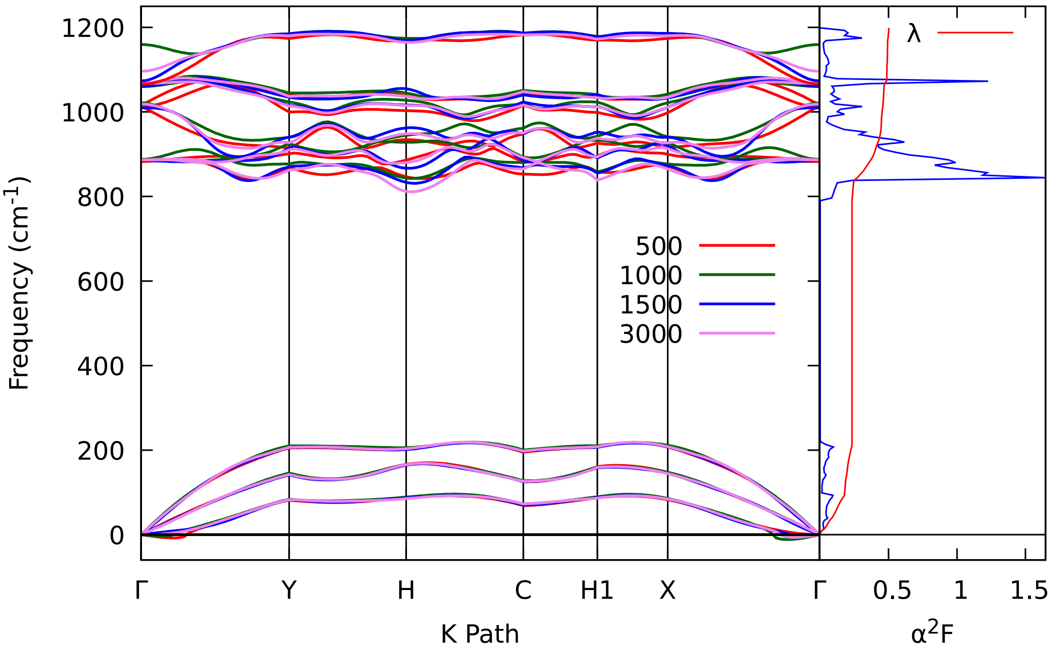

Figure 5.5: H_2Pd phonon spectra for 4 different values of k-point densities, namely 500, 1000, 1500 and 3000. The Eliashberg spectral function, α^2F (in blue), and λ (in red) are shown for the 1500 case.

5.3 TiTeS

This material composed of titanium, tellurium and sulfur belongs to the hexagonal crystal system shown in Figure 5.6 with a lattice parameter of 3.52 Å. The crystal structure is shown in Figure 5.8 where the yellow, blue and brown atoms represent the sulfur, titanium and tellurium elements respectively. The atoms arrange themselves in three planes with the sulfur atoms 1.23 Å above the titanium ones. The tellurium atoms are the lowest plane, 1.89 Å below the middle titanium plane. The band structure and density of states can be seen in Figure 5.9. The obtained phonon frequencies, the Eliashberg spectral function (in blue) and the integrated coupling constant λ (in red) for a kppa of 3000 is shown in Figure 5.10. The obtained λ, ω_{log} and consequently T_{c} are shown in Table 5.1.

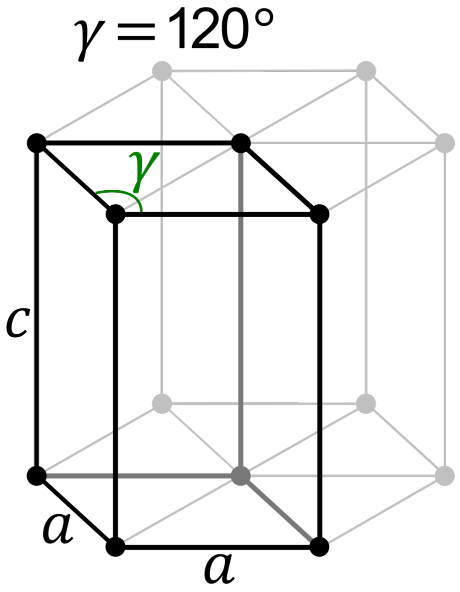

Figure 5.6: Hexagonal crystal system unit cell.

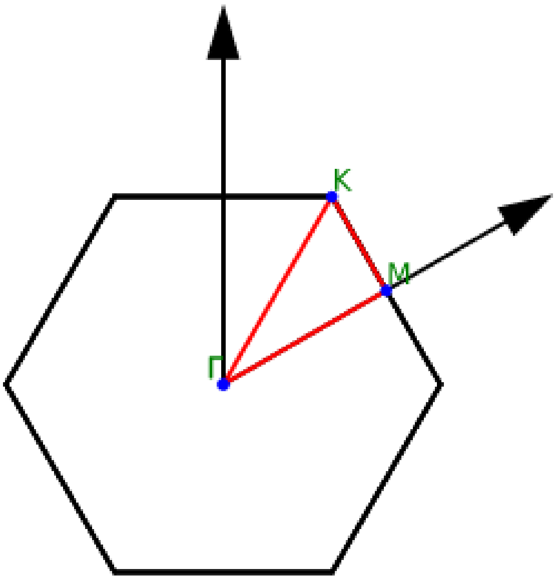

Figure 5.7: TiTeS Brillouin zone with the path along high-symmetry points highlighted.

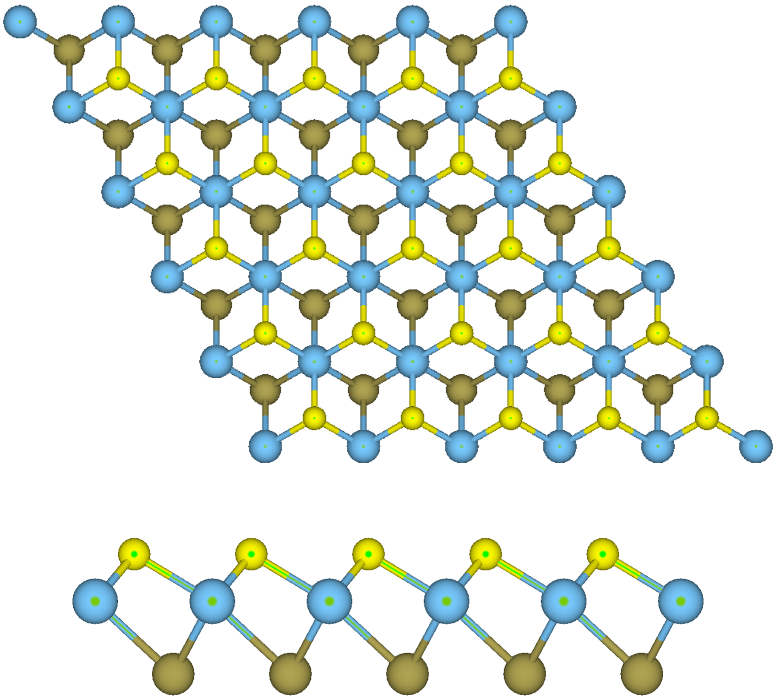

Figure 5.8: TiTeS material visualized from the z (top panel) and x (bottom panel) directions respectively.

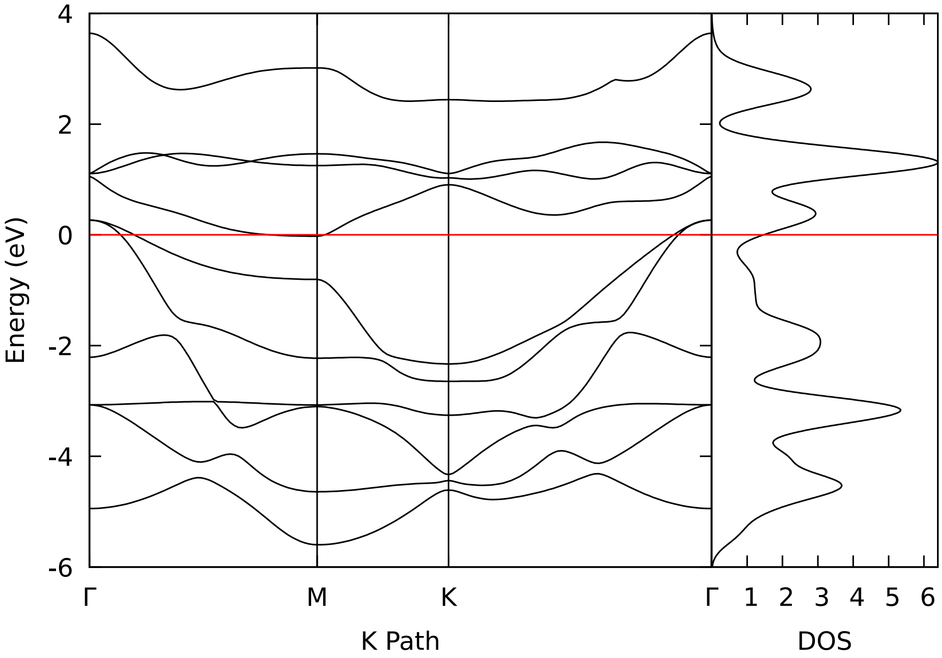

Figure 5.9: Electronic band structure and density of states (DOS) of TiTeS.

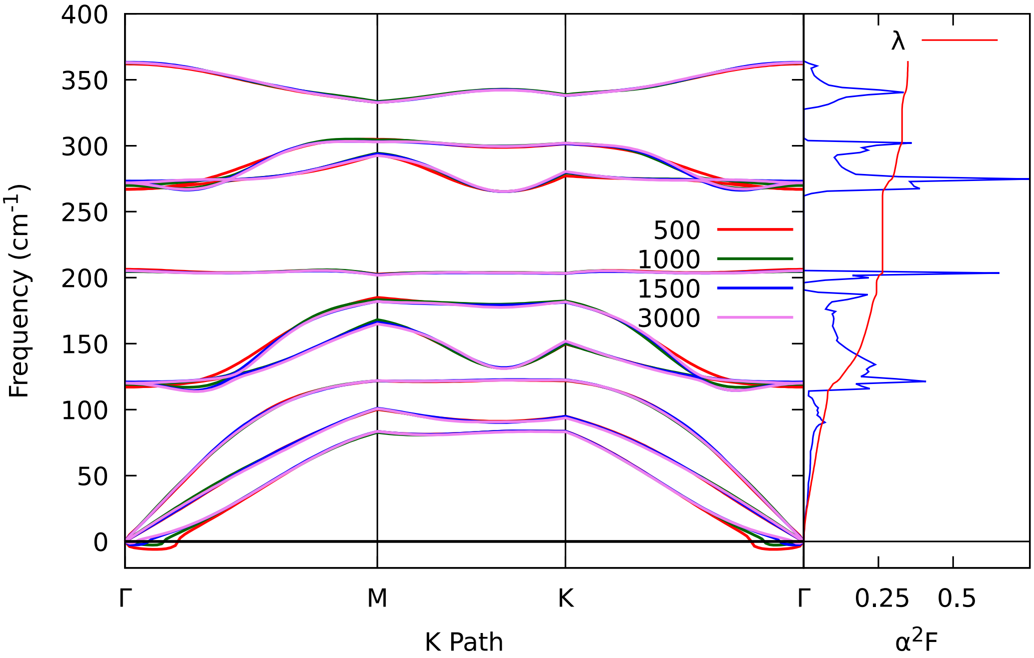

Figure 5.10: TiTeS phonon spectra for 4 different values of k-point densities, namely 500, 1000, 1500 and 3000. The Eliashberg spectral function, $\alpha^2 F$ (in blue), and λ (in red) are shown for the 1500 case.

5.4 Tl_2Pb

The Tl_2Pb cell is of the monoclinic type with lattice parameters a of 4.69 Å and b 6.71 Å, and forming an angle of 135°.

The material's structure can be seen in Figure 5.13 where the grey atoms are lead while the beige ones represent the thallium atoms. In this material the thallium atoms' plane sits 2.61 Å above and below the lead plane. From this arrangement of the atoms the band structure and density of states obtained can be seen in Figure 5.14 and the phonon dispersion curves with the Eliashberg spectral function (in blue) and the integrated coupling constant λ (in red) are shown in Figure 5.15. This material took the longest to run calculations on, this can be explained by the massive atoms with many electrons present in its structure as well as the low symmetry of it's unit cell compared to the other materials.

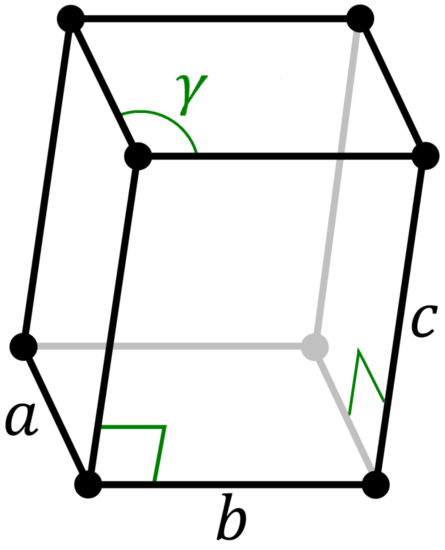

Figure 5.11: Monoclinic crystal system unit cell.

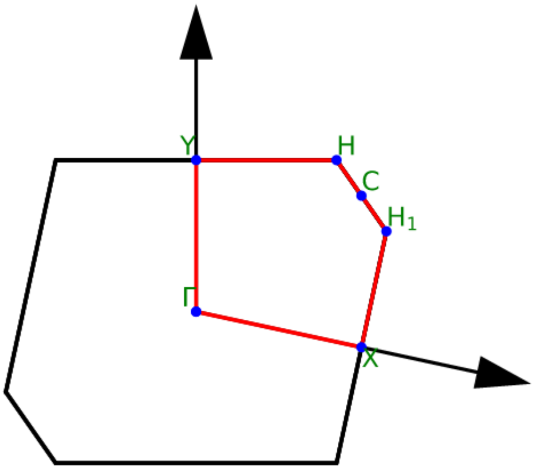

Figure 5.12: Tl_2Pb Brillouin zone with the path along high-symmetry points highlighted.

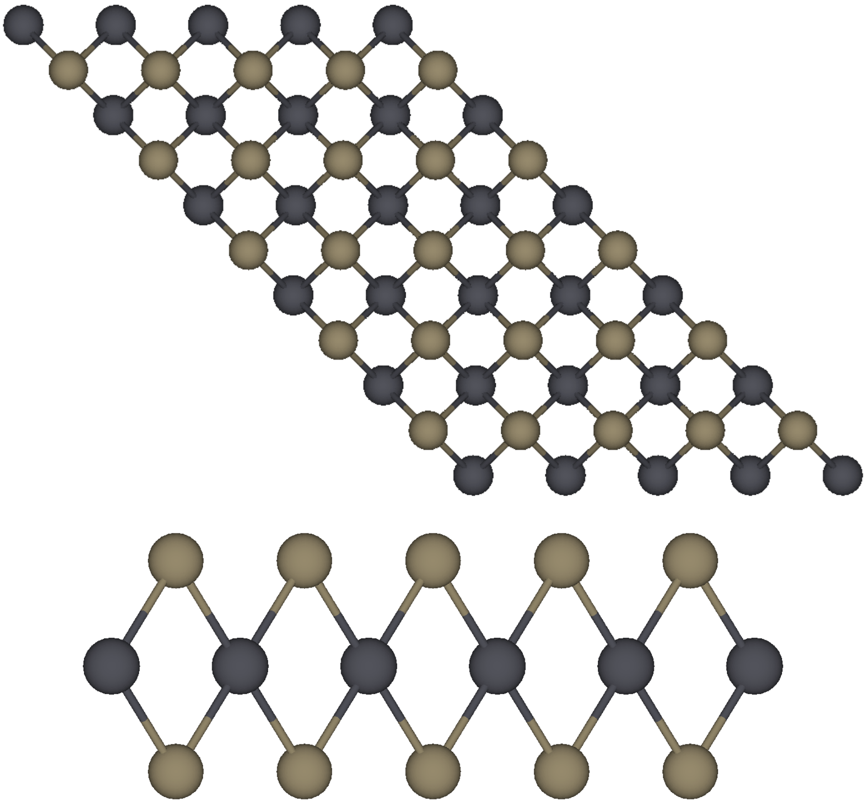

Figure 5.13: Tl_2Pb material visualized from the z (top panel) and x (bottom panel) directions respectively.

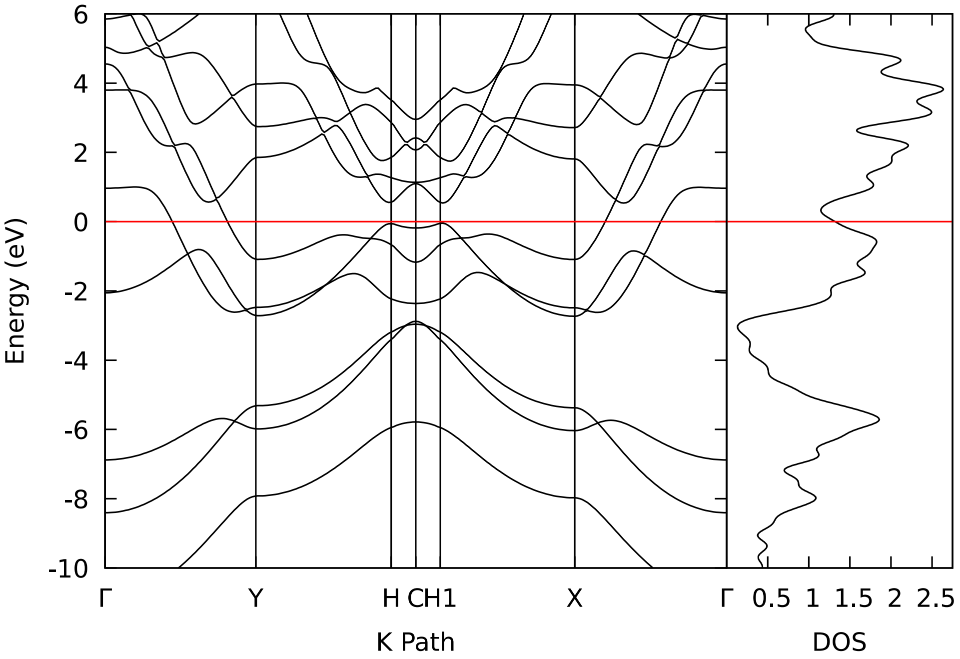

Figure 5.14: Electronic band structure and density of states (DOS) of Tl_2Pb.

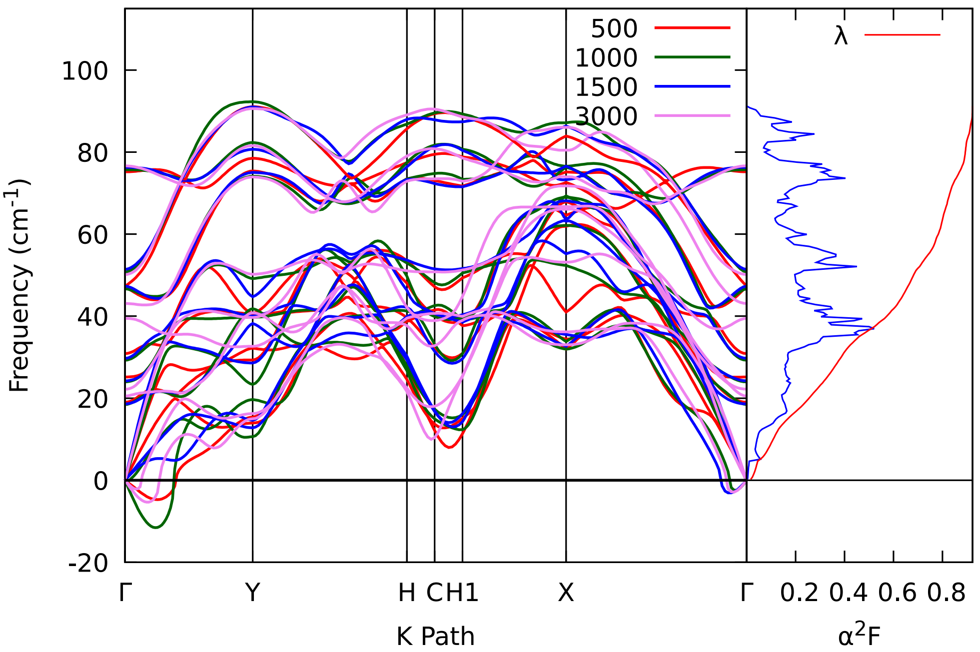

Figure 5.15: Tl_2Pb phonon spectrum for 4 different kppa values of 500, 1000 and 1500. The spectral function $\alpha^2 F$ and λ shown are for the kppa=1500 case.

5.5 NiS

This material forms an hexagonal unit cell with vector a lattice parameter a of length 3.55 Å containing two nickel and two sulfur atoms inside it. In Figure 5.18 the yellow atoms are sulfur and the grey ones are nickel. These atoms arrange themselves in two hexagons with alternating nickel and sulfur atoms. These two hexagons are stacked on top of each other at a distance of 2.20 Å, with the alternating nickel and sulfur atoms of each layer having a height difference of 0.71 Å. The Brillouin zone in Figure 5.17 shows the reciprocal vectors and the path considered when making the band structure and density of states plot shown in Figure 5.20 as well as the phonon frequencies with the Eliashberg spectral function (in blue) and the integrated coupling constant λ (in red) in Figure 5.20.

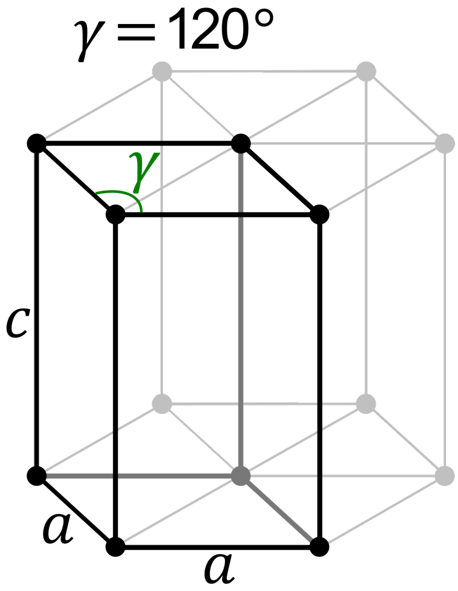

Figure 5.16: Hexagonal crystal system unit cell.

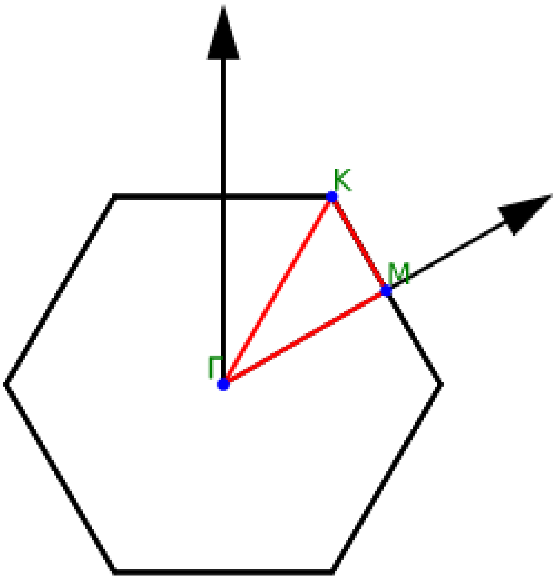

Figure 5.17: NiS Brillouin zone with the path along high-symmetry points highlighted.

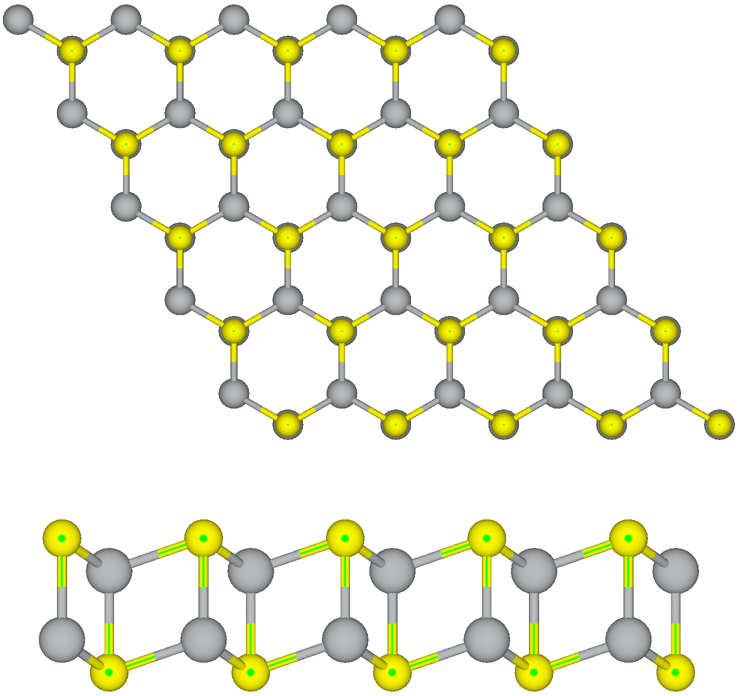

Figure 5.18: NiS material visualized from the z (top panel) and x (bottom panel) directions respectively.

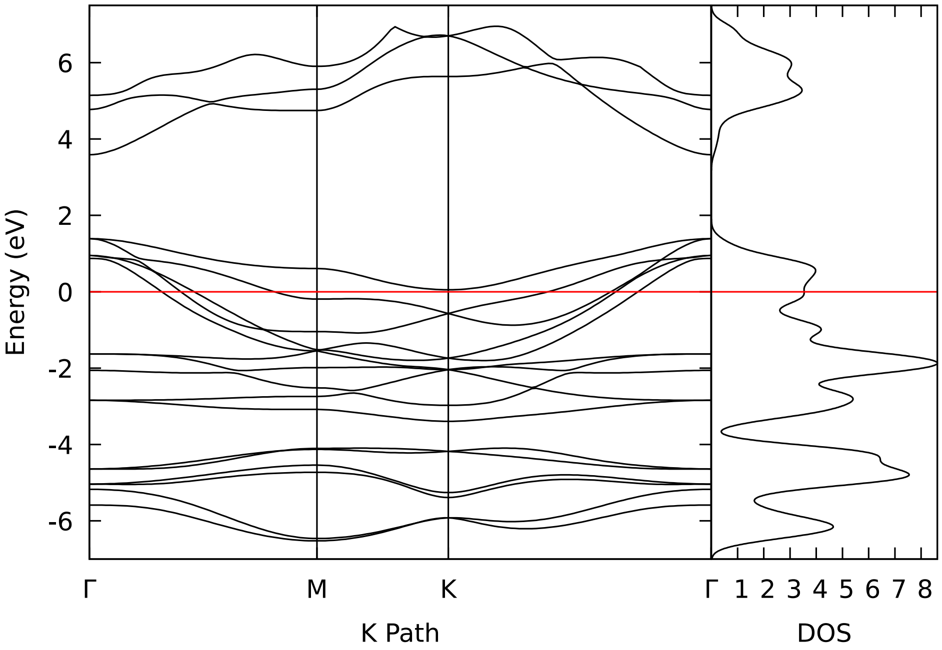

Figure 5.19: Electronic band structure and density of states (DOS) of NiS.

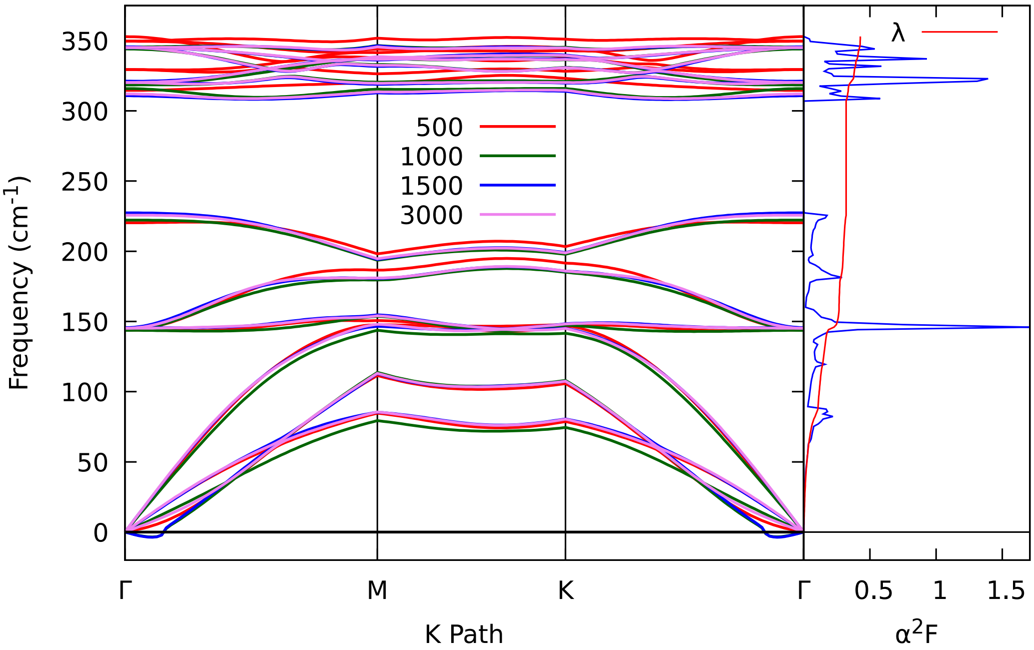

Figure 5.20: NiS phonon spectrum for 4 different kppa values of 500, 1000, 1500 and 3000. The spectral function α^2F and λ shown are for the kppa=1500 case.

5.6 $CuAgTe_2$

This material forms in an orthorhombic lattice shown in Figure 5.21 with four atoms in its unit cell. In this unit cell the lattice parameter a has a length of 3.14 Å while the b lattice parameter has length 4.15 Å. In the structure shown in Figure 5.23 the grey atoms represent silver while the blue ones represent copper and the beige atoms tellurium. This structure can be viewed as two layers, a top layer with alternating copper and tellurium atoms with a height difference of 1.62 Å between them and a bottom layer with alternating silver and tellurium atoms with a height difference of 1.74 Å between them. Both layers are separated by a distance of 2.42 Å. The obtained band structure and density of states is shown in Figure 5.24. The phonon spectrum with the Eliashberg spectral function (in blue) and the integrated coupling constant λ (in red) in shown in Figure 5.25. From this plot we can see the presence of multiple imaginary modes, indicating that it is not dynamically stable. These imaginary modes were obtained in all runs regardless of the grid, and other parameters used.

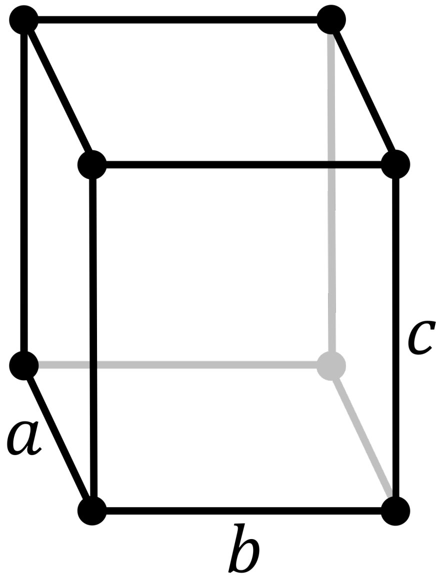

Figure 5.21: Orthorhombic crystal system unit cell.

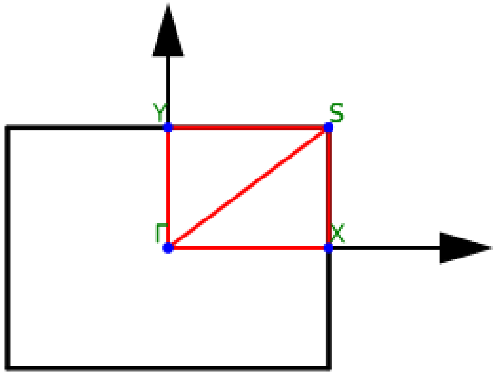

Figure 5.22: $CuAgTe_2$ Brillouin zone with the path along high-symmetry points highlighted.

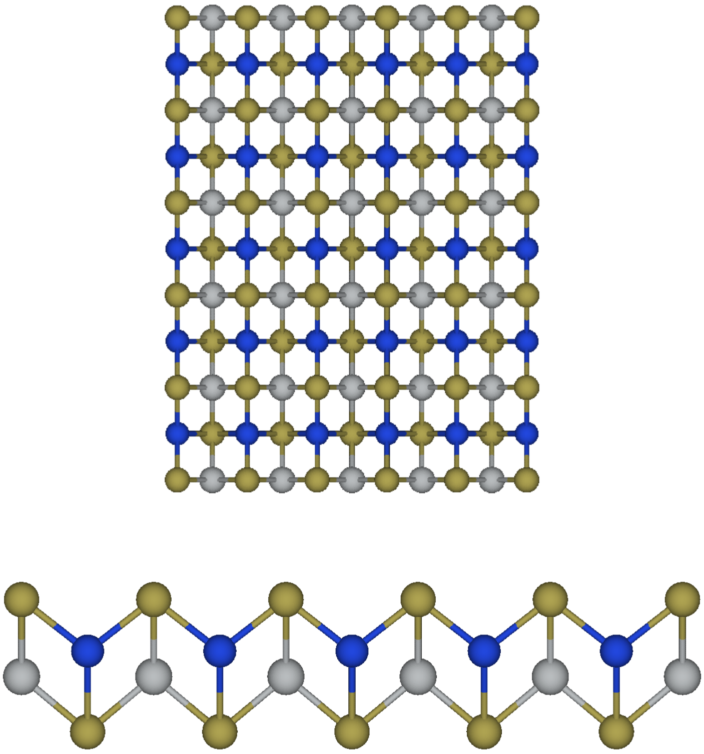

Figure 5.23: $CuAgTe_2$ material visualized from the z (top panel) and x (bottom panel) directions respectively.

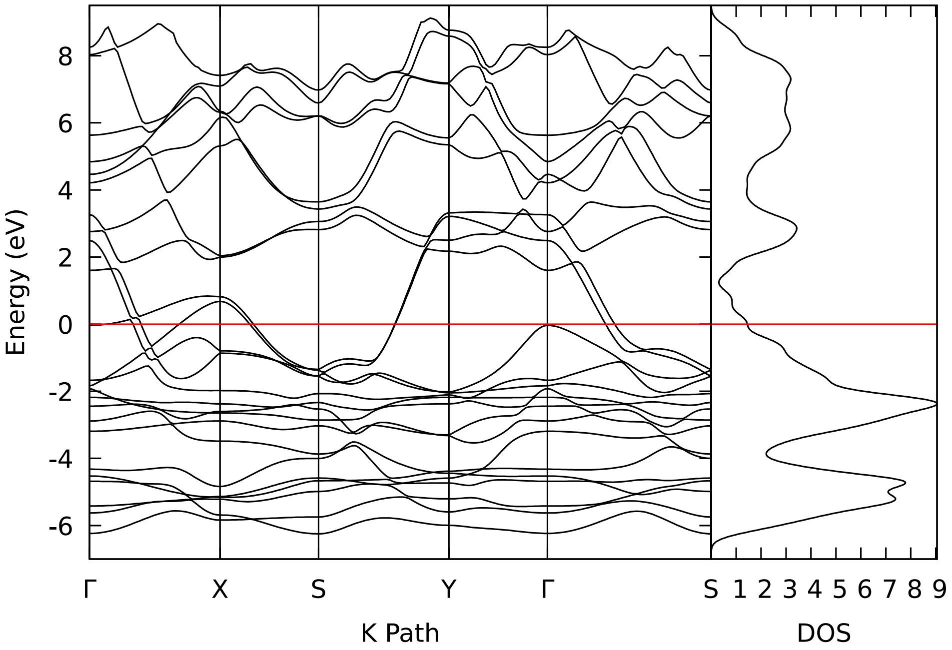

Figure 5.24: Electronic band structure and density of states (DOS) of $CuAgTe_2$.

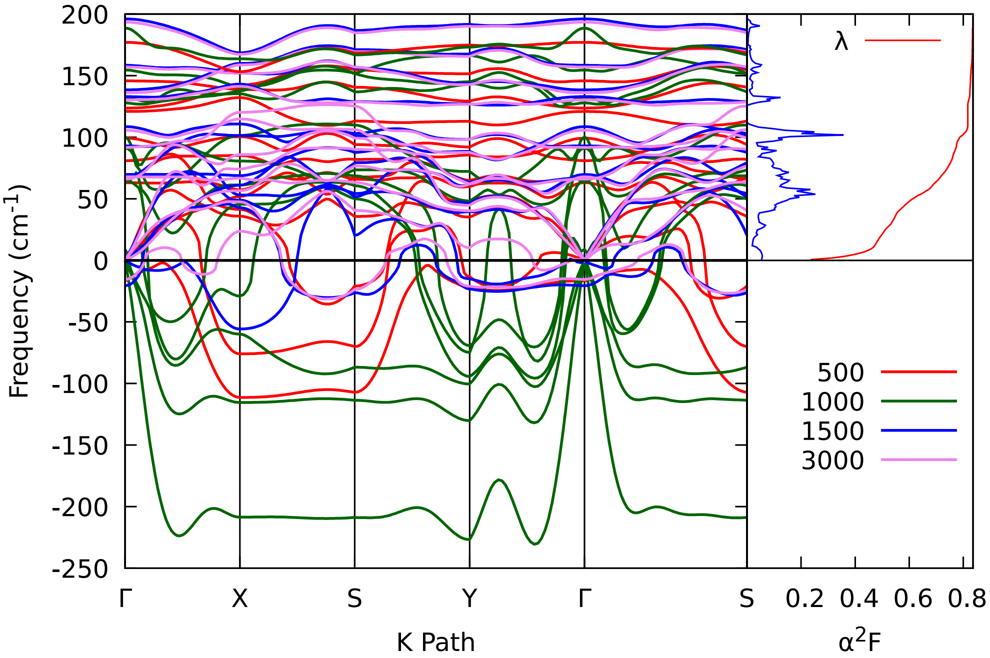

Figure 5.25: $CuAgTe_2$ phonon spectrum for 4 different kppa values of 500, 1000, 1500 and 3000. The spectral function α^2F and λ shown are for the kppa=1500 case.

5.7 Discussion

From the results of Table 5.1 we can see that four materials belong to the weak coupling regime $\lambda \sim 0.4$ with Tl_2Pb being the exception ($\lambda \sim 0.9$). Also noticeable is the fact that some materials' parameters (λ and ω_{log}) and T_{c} converge rather rapidly (for example TiTeS and NiS) while for other materials the values oscillate more. For most of the studied materials we see that the obtained transition temperature converges at a kppa value of 1500. The transition temperatures for different kppa values of each material oscillate on average 30% with respect to the last performed run (kppa=3000). Due to the low transition temperatures obtained these oscillations amount mostly to less than 1K. Mostly even with a kppa of 1000, we already get values close to the converged value. However, as the materials chosen all have relatively low T_{c}'s, this conclusion may not be general, and further tests are needed. Sadly, all these materials studied here have very low transition temperatures and do not show promise as practical superconductors.

Material	Kppa	k-grid	λ	ω_{log}(K)	T_{c}(K)
H_2Pd	500	10x10x1	0.44	623.1	4.5
H_2Pd	1000	12x12x2	0.42	450.9	2.6
H_2Pd	1500	14x14x2	0.51	367.7	4.8
H_2Pd	3000	18x18x4	0.44	483.7	3.4
TiTeS	500	10x10x1	0.35	187.2	0.3
TiTeS	1000	12x12x2	0.34	206.0	0.3
TiTeS	1500	14x14x2	0.35	200.2	0.3
TiTeS	3000	18x18x4	0.35	203.0	0.4
Tl_2Pb	500	12x8x1	1.03	39.8	2.9
Tl_2Pb	1000	14x10x2	0.9	45.8	2.7
Tl_2Pb	1500	16x12x2	0.87	46.0	2.5
Tl_2Pb	3000	20x14x4	0.82	50.3	2.5
Ni_2S_2	500	8x8x1	0.41	221.0	1.0
Ni_2S_2	1000	10x10x2	0.45	193.1	1.5
Ni_2S_2	1500	12x12x2	0.44	209.7	1.4
Ni_2S_2	3000	16x16x4	0.43	224.1	1.4
$CuAgTe_2$	500	10x8x1	0.56	49.2	0.9
$CuAgTe_2$	1000	12x10x2	0.44	43.5	0.3
$CuAgTe_2$	1500	14x10x2	0.43	57.1	0.4
$CuAgTe_2$	3000	18x14x2	0.44	53.4	0.4

Table 5.1: Table of results listing from left to right the material, k-points per reciprocal atom (kppa), the corresponding grid of k points used, the superconducting coupling parameters λ, ω_{log} and finally the critical transition temperature obtained with equation 2.87.

Chapter 6

Conclusions and Future Work

In this work the band structure, density of states, phonon's frequency spectrum with the density of states, electron-phonon coupling constant, logarithmic frequency average and critical temperature to transition to a superconductor were obtained for five novel 2D materials. From this work we can conclude that relatively small kppa values are enough to screen a 2D material's electron-phonon coupling constants and obtain a good estimate for its critical transition temperature.

These grids give a good estimate for the λ and $\omega_{\log}$ and are sufficient to obtain good results, doing so more quickly than larger grids. The five novel materials approached in this work show transition temperatures between 0.4K and 3K. Of these five materials, three belonged to the weak coupling regime ($\lambda \sim 0.4$) with the material Tl_2Pb having the highest value. In the $CuAgTe_2$ case, all the runs performed show imaginary frequencies, which indicates that it is not dynamically stable.

As aforementioned, in the motivation, this whole process can be scripted thus allowing an automated and hands-off search for novel 2D superconductors.

References

[1] H. Kamerlingh. Onnes. Further experiments with liquid helium. g. on the electrical resistance of pure metals, etc. vi on the sudden change in the rate at which the resistance of mercury disappears. *Communications Leiden 124c*, Nov 1911.

[2] K. S. Novoselov, A. K. Geim, S. V. Morozov, D. Jiang, Y. Zhang, S. V. Dubonos, I. V. Grigorieva, and A. A. Firsov. Electric field effect in atomically thin carbon films. *Science*, 306(5696):666–669, oct 2004.

[3] Mariyappan Shanmugam, Robin Jacobs-Gedrim, Eui Sang Song, and Bin Yu. Two-dimensional layered semiconductor/graphene heterostructures for solar photovoltaic applications. *Nanoscale*, 6:12682–12689, 2014.

[4] Peder Lyngby and Kristian Sommer Thygesen. Data-driven discovery of 2d materials by deep generative models. *npj Computational Materials*, 8(1), nov 2022.

[5] Hai-Chen Wang, Jonathan Schmidt, Miguel A. L. Marques, Ludger Wirtz, and Aldo H. Romero. Symmetry-based computational search for novel binary and ternary 2d materials, 2023.

[6] M. Born and R. Oppenheimer. Zur quantentheorie der molekeln. *Annalen der Physik*, 389(20):457–484, 1927.

[7] P. Hohenberg and W. Kohn. Inhomogeneous electron gas. *Phys. Rev.*, 136:B864–B871, Nov 1964.

[8] W. Kohn and L. J. Sham. Self-consistent equations including exchange and correlation effects. *Phys. Rev.*, 140:A1133–A1138, Nov 1965.

[9] Mel Levy. Electron densities in search of hamiltonians. *Phys. Rev. A*, 26:1200–1208, Sep 1982.

[10] Shimony A. Feshbach H. Tisza, L. and Lieb E.H. *Density Functionals for Coulomb Systems.* Physics as Natural Philosophy: Essays in Honor of Laszlo Tisza on His Seventy-Fifth Birthday. MIT Press Ltd, 1982.

[11] John P. Perdew and Karla Schmidt. Jacob's ladder of density functional approximations for the exchange-correlation energy. *AIP Conference Proceedings*, 577(1):1–20, 07 2001.

[12] P. A. M. Dirac. Note on exchange phenomena in the thomas atom. *Mathematical Proceedings of the Cambridge Philosophical Society*, 26(3):376–385, 1930.

[13] D. M. Ceperley and B. J. Alder. Ground state of the electron gas by a stochastic method. *Phys. Rev. Lett.*, 45:566–569, Aug 1980.

[14] S. H. Vosko and L. Wilk. Influence of an improved local-spin-density correlation-energy functional on the cohesive energy of alkali metals. *Phys. Rev. B*, 22:3812–3815, Oct 1980.

[15] John P. Perdew, J. A. Chevary, S. H. Vosko, Koblar A. Jackson, Mark R. Pederson, D. J. Singh, and Carlos Fiolhais. Atoms, molecules, solids, and surfaces: Applications of the generalized gradient approximation for exchange and correlation. *Phys. Rev. B*, 46:6671–6687, Sep 1992.

[16] Axel D. Becke. Density-functional thermochemistry. I. The effect of the exchange-only gradient correction. *The Journal of Chemical Physics*, 96(3):2155–2160, 02 1992.

[17] E. I. Proynov, E. Ruiz, A. Vela, and D. R. Salahub. Determining and extending the domain of exchange and correlation functionals. *International Journal of Quantum Chemistry*, 56(S29):61–78, 1995.

[18] B. Hammer, K. W. Jacobsen, and J. K. Nørskov. Role of nonlocal exchange correlation in activated adsorption. *Phys. Rev. Lett.*, 70:3971–3974, Jun 1993.

[19] D. R. Hamann. Generalized gradient theory for silica phase transitions. *Phys. Rev. Lett.*, 76:660–663, Jan 1996.

[20] SHANG-kENG MA and KEITH A. BRUECKNER. Correlation energy of an electron gas with a slowly varying high density. *Phys. Rev.*, 165:18–31, Jan 1968.

[21] John P. Perdew, Adrienn Ruzsinszky, Gábor I. Csonka, Oleg A. Vydrov, Gustavo E. Scuseria, Lucian A. Constantin, Xiaolan Zhou, and Kieron Burke. Restoring the density-gradient expansion for exchange in solids and surfaces. *Physical Review Letters*, 100(13), apr 2008.

[22] B. T. Matthias, T. H. Geballe, S. Geller, and E. Corenzwit. Superconductivity of nb$_3$sn. *Phys. Rev.*, 95:1435–1435, Sep 1954.

[23] T. G. Berlincourt and R. R. Hake. Superconductivity at high magnetic fields. *Phys. Rev.*, 131:140–157, Jul 1963.

[24] J G Bednorz and K A Müller. Possible hightc superconductivity in the BaLaCuO system. *Zeitschrift für Physik B Condensed Matter*, 64(2):189–193, June 1986.

[25] J. Bardeen, L. N. Cooper, and J. R. Schrieffer. Theory of superconductivity. *Phys. Rev.*, 108:1175–1204, Dec 1957.

[26] Neil Ashcroft and David Mermin. *Solid State Physics*, volume 46. 01 1976.

[27] Philip B. Allen and Božidar Mitrović. Theory of superconducting tc. 37:1–92, 1983.

[28] José Flores-Livas, Lilia Boeri, Antonio Sanna, Gianni Profeta, Ryotaro Arita, and Mikhail Eremets. A perspective on conventional high-temperature superconductors at high pressure: Methods and materials. *Physics Reports*, 856, 02 2020.

[29] G M Eliashberg. Interactions between electrons and lattice vibrations in a superconductor. *Sov. Phys. - JETP (Engl. Transl.); (United States)*, 3(11), 9 1960.

[30] P. Morel and P. W. Anderson. Calculation of the superconducting state parameters with retarded electron-phonon interaction. *Phys. Rev.*, 125:1263–1271, Feb 1962.

[31] W. L. McMillan. Transition temperature of strong-coupled superconductors. *Phys. Rev.*, 167:331–344, Mar 1968.

[32] R.C. Dynes. Mcmillan's equation and the tc of superconductors. *Solid State Communications*, 10(7):615–618, 1972.

[33] Zixin Xiong, Lei Zhong, Haotian Wang, and Xiaoyan Li. Structural defects, mechanical behaviors, and properties of two-dimensional materials. *Materials*, 14(5), 2021.

[34] Alexander A et al. Balandin. Superior thermal conductivity of Single-Layer graphene. *Nano Lett.*, 8(3):902–907, March 2008.

[35] Hang Chen, Guangbao Mi, Peijie Li, Xu Huang, and Chunxiao Cao. Microstructure and tensile properties of graphene-oxide-reinforced high-temperature titanium-alloy-matrix composites. *Materials*, 13:3358, 07 2020.

[36] Yuan Cao, Valla Fatemi, Shiang Fang, Kenji Watanabe, Takashi Taniguchi, Efthimios Kaxiras, and Pablo Jarillo-Herrero. Unconventional superconductivity in magic-angle graphene superlattices. *Nature*, 556(7699):43–50, mar 2018.

[37] Xiao Li and Hongwei Zhu. Two-dimensional mos2: Properties, preparation, and applications. *Journal of Materiomics*, 1(1):33–44, 2015.

[38] Daniel Wines, Kamal Choudhary, Adam J. Biacchi, Kevin F. Garrity, and Francesca Tavazza. High-throughput dft-based discovery of next generation two-dimensional (2d) superconductors. *Nano Letters*, 23(3):969–978, 2023. PMID: 36715314.

[39] Thibault Sohier, Matteo Calandra, and Francesco Mauri. Density functional perturbation theory for gated two-dimensional heterostructures: Theoretical developments and application to flexural phonons in graphene. *Phys. Rev. B*, 96:075448, Aug 2017.

[40] Thibault Sohier, Marco Gibertini, Matteo Calandra, Francesco Mauri, and Nicola Marzari. Breakdown of optical phonons' splitting in two-dimensional materials. *Nano Letters*, 17(6):6. 3758–3763, 2017.

[41] Jesús Carrete, Wu Li, Lucas Lindsay, David A. Broido, Luis J. Gallego, and Natalio Mingo. Physically founded phonon dispersions of few-layer materials and the case of borophene. *Materials Research Letters*, 4(4):204–211, 2016.

[42] IM Lifshitz. On thermal properties of chained and layered structures at low temperatures (in russian). *Zh. Éksp. Teor. Fiz.*, 22(4):475–486, 1952.

[43] Xavier Gonze, Gian-Marco Rignanese, and Razvan Caracas. First-principle studies of the lattice dynamics of crystals, and related properties. *Zeitschrift für Kristallographie - Crystalline Materials*, 220(5-6):458–472, 2005.

[44] L.A. Falkovsky. Symmetry constraints on phonon dispersion in graphene. *Physics Letters A*, 372(31):5189–5192, 2008.

[45] Paolo Giannozzi et al. QUANTUM ESPRESSO: a modular and open-source software project for quantum simulations of materials. *Journal of Physics: Condensed Matter*, 21(39):395502, sep 2009.

[46] M.J. van Setten, M. Giantomassi, E. Bousquet, M.J. Verstraete, D.R. Hamann, X. Gonze, and G.-M. Rignanese. The PseudoDojo: Training and grading a 85 element optimized norm-conserving pseudopotential table. *Computer Physics Communications*, 226:39–54, may 2018.

[47] Ask Hjorth Larsen et al. The atomic simulation environment—a python library for working with atoms. *Journal of Physics: Condensed Matter*, 29(27):273002, jun 2017.

[48] Koichi Momma and Fujio Izumi. Vesta: A three-dimensional visualization system for electronic and structural analysis. *Journal of Applied Crystallography - J APPL CRYST*, 41:653–658, 06 2008.

[49] Yanlong Ding, Shuiquan Deng, and Yong Zhao. The electronic structure of nb3al/nb3sn, a new test case for flat/steep band model of superconductivity. *Journal of Modern Transportation*, 22(3):183–186, Sep 2014.

[50] Materials Project. Nb3sn mp-1326, 2023. https://next-gen.materialsproject.org/materials/mp-1326?formula=Nb3Sn [Accessed: 25/07/2023].

[51] Gianluca De Marzi, L. Morici, and Luigi Muzzi. Ab-initio calculations of nb3sn superconducting properties under applied mechanical strain. 03 2014.

[52] Jun Dai, Zhenyu Li, Jinlong Yang, and Jianguo Hou. A first-principles prediction of two-dimensional superconductivity in pristine b2c single layers. *Nanoscale*, 4:3032–3035, 2012.

[53] Shyue Ping Ong, William Davidson Richards, Anubhav Jain, Geoffroy Hautier, Michael Kocher, Shreyas Cholia, Dan Gunter, Vincent L. Chevrier, Kristin A. Persson, and Gerbrand Ceder. Python materials genomics (pymatgen): A robust, open-source python library for materials analysis. *Computational Materials Science*, 68:314–319, 2013.